









Coexisting single-particle excitations and octupole correlations in the transitional nucleus  $^{217}\text{Ra}$ 

Madhu,<sup>1</sup> A. Y. Deo <sup>1,\*</sup>, Khamosh Yadav <sup>1</sup>, Dhananjaya Sahoo <sup>1</sup>, Y. Y. Wang,<sup>2</sup> Y. K. Wang,<sup>3</sup> J. Meng <sup>3,4</sup>, Saket Suman <sup>5</sup>, S. K. Tandel <sup>5</sup>, A. Sharma,<sup>6</sup> I. Ahmed <sup>7</sup>, K. Katre,<sup>7</sup> K. Rojeeta Devi,<sup>7</sup> S. Dutt,<sup>7</sup> S. Kumar,<sup>7</sup> Yashraj,<sup>7</sup> S. Muralithar,<sup>7</sup> and R. P. Singh <sup>7</sup>

<sup>1</sup>Department of Physics, Indian Institute of Technology Roorkee, Roorkee 247667, India

<sup>2</sup>Mathematics and Physics Department, North China Electric Power University, Beijing 102206, China

<sup>3</sup>State Key Laboratory of Nuclear Physics and Technology, School of Physics, Peking University, Beijing 100871, China

<sup>4</sup>Yukawa Institute for Theoretical Physics, Kyoto University, Kyoto 606-8502, Japan

<sup>5</sup>School of Physical Sciences, UM-DAE Centre for Excellence in Basic Sciences, University of Mumbai, Mumbai 400098, India

<sup>6</sup>Department of Physics, Himachal Pradesh University, Shimla 171005, India

<sup>7</sup>Inter University Accelerator Centre, Aruna Asaf Ali Marg, New Delhi 110067, India



(Received 3 April 2023; revised 17 May 2023; accepted 27 June 2023; published 6 July 2023)

The level structure of the transitional nucleus  $^{217}\text{Ra}$  has been extended with the addition of around 20 new transitions. The discrepancies between the placements of several transitions reported in the earlier studies are resolved. The newly established negative-parity sequence at low excitation energies hints at the expected parity-doublet structures in this nucleus. The properties of the observed simplex bands are compared with that of similar bands in neighboring nuclei. Since the presence of parity-doublet structures reflects octupole correlations, theoretical calculations using reflection-asymmetric triaxial particle rotor model (RAT-PRM) have been performed. A comparison of the observed features of the simplex bands with the predictions of the RAT-PRM calculations suggests that  $^{217}\text{Ra}$  exhibits an intermediate behavior between the extremes of spherical and octupole-deformed nuclei. The termination of the simplex bands at intermediate energies and the structures lying above reflect the dominance of the single-particle excitations at higher excitation energies.

DOI: [10.1103/PhysRevC.108.014309](https://doi.org/10.1103/PhysRevC.108.014309)

## I. INTRODUCTION

The atomic nucleus is a many-body quantal system in which the number of valence nucleons outside the shell closure and the interactions between them mainly govern shape and properties of the system. At the beginning of several major shells, the presence of an opposite-parity intruder orbital in the vicinity of normal-parity orbitals with  $\Delta j = \Delta l = 3$  gives rise to long-range octupole correlations between the valence nucleons [1]. Such orbitals are present near the Fermi surface in nuclei with  $Z$  or  $N \simeq 34, 56, 88,$  and  $134$  where the fingerprints of dynamical or stable reflection asymmetric shapes have been observed [1–3]. The advancements in the experimental facilities with the availability of radioactive ion beams and targets have facilitated the measurements of the  $E3$  transition strengths using Coulomb excitation techniques [4–8]. The deduced electric octupole moments, which are a direct measure of the strength of octupole correlations, in the Ra isotopes with  $134 \leq N \leq 138$  ( $^{222}\text{Ra}$ ,  $^{224}\text{Ra}$ ,  $^{226}\text{Ra}$ ) have confirmed the stable octupole deformation in these nuclei [4–6,9]. In terms of the level structures, static quadrupole and octupole deformation in the even-even nuclei is characterized by  $\Delta I = 2$  sequences of opposite parities connected by enhanced  $E1$  transitions. The excitation energies of the states of these  $\Delta I = 2$  bands follow the  $I(I + 1)$  dependence

as expected for rotational bands. Also, the negative-parity sequence is expected to be perfectly interleaved with the positive-parity ground state band in the case of static octupole deformation. In addition, the typical  $B(E1)/B(E2)$  ratios are of the order of  $\approx 10^{-6} \text{ fm}^{-2}$  for such nuclei [1–3]. For the case of odd- $A$  and doubly odd nuclei where the odd nucleon tilts the total angular momentum with respect to the normal to the symmetry plane, the simplex symmetry is broken [10]. In such nuclei, parity-doublet structures (almost degenerate states of the same spin but opposite parity) are expected [1,10].

As one moves away from the region of stable octupole deformation toward the shell closure, a transitional region is encountered where the interplay between both the single-particle and collective degrees of freedom results in complex structures and the properties mentioned above become less pronounced. The recent high-spin investigations in  $N = 130$  isotones ( $^{218}\text{Ra}$  and  $^{220}\text{Th}$ ) and  $^{219}\text{Th}$  report near-constant transition energies and spin-dependent staggering of  $B(E1)/B(E2)$  ratios in these nuclei [11–13]. The almost constant level spacings and angular velocity over a spin range imply that the nucleus does not gain angular momentum by rotating faster. Thus, a new approach in terms of a reflection asymmetric tidal wave running over the nuclear surface has been proposed to interpret the observed properties in these nuclei [14].

It has been noted that the properties of the level structures of nuclei in the transitional region exhibit a significant

\*ajay.deo@ph.iitr.ac.in

dependence on the nucleon number. The low-lying states in  $^{216}\text{Ra}$ , with two valence neutrons outside the shell closure, exhibit decreasing level spacing with spin as expected for single-particle  $\nu g_{9/2}^+$  excitations [15,16]. On the other hand, spectroscopic studies in  $^{218}\text{Ra}$  ( $N = 130$ ) revealed irregular sequences of opposite parity connected by enhanced  $E1$  transitions which, in turn, reflect the dominance of octupole correlations over quadrupole deformation in this nucleus [17]. In  $^{217}\text{Ra}$ , which lies in between the above mentioned isotopes, three sequences of  $E2$  transitions are reported at low excitation energies out of which two are connected by  $E1$  transitions [18–21]. Although the alternating parity sequence was qualitatively understood in terms of single-particle neutron excitations, the observed near linear spin dependence of excitation energies and large  $B(E1)/B(E2)$  ratios ( $\approx 10^{-6} \text{ fm}^{-2}$ ) hint at the contribution of collective degrees of freedom in this nucleus. Thus, the disparate level structure in  $^{217}\text{Ra}$  with respect to its neighboring even-even isotopes requires a detailed spectroscopic study of this nucleus to understand how the dominance of underlying degrees of freedom evolves in the transitional region.

Prior to the present work, excited states in  $^{217}\text{Ra}$  were established using the in-beam  $\gamma$ -ray and conversion-electron spectroscopy along with the  $\alpha$ -decay studies [18–24]. It was observed that the placement and ordering of several transitions were at variance in the in-beam studies and need to be revisited [18–21]. Also, the spin-parities of the excited states above 2.4 MeV energy were reported to be tentative in these studies. It may be noted that the low-lying level structure in  $^{217}\text{Ra}$  is observed to be similar to its  $N = 129$  isotones [13,25,26]. However, in all the  $N = 129$  isotones with  $87 \leq Z \leq 90$  nuclei, except  $^{217}\text{Ra}$ , parity-doublet structures have been reported. Therefore, it is imperative to search for similar structures expected in  $^{217}\text{Ra}$  and understand the observed properties with the help of the relevant nuclear models. Thus, an extensive  $\gamma$ -ray spectroscopy study of  $^{217}\text{Ra}$  has been carried out using the heavy-ion fusion reaction mechanism to investigate high-spin states and the evolution of structure with angular momentum in this nucleus. In the present work, we report an extended level scheme of  $^{217}\text{Ra}$  with the addition of around 20 new transitions. We provide the first evidence of a new negative-parity sequence which constitutes the simplex partner band of the already reported ground state alternating parity sequence. Also, the observed level structures in  $^{217}\text{Ra}$  reflect the coexistence of single-particle and collective excitations in this transitional nucleus.

## II. EXPERIMENTAL DETAILS

High-spin states in  $^{217}\text{Ra}$  were populated using the  $^{208}\text{Pb}(^{12}\text{C}, 3n)^{217}\text{Ra}$  reaction. The  $^{12}\text{C}$  beam with 68-, 72-, and 80-MeV energies was provided by the 15UD Pelletron accelerator at the Inter-University Accelerator Centre, New Delhi. The target consisted of an isotopically enriched (99%) and self-supporting  $^{208}\text{Pb}$  foil of  $\approx 9 \text{ mg/cm}^2$  thickness. The  $\gamma$  rays deexciting the residual nuclei were detected using the Indian National Gamma Array (INGA) [27] comprising 13 Compton suppressed clover detectors and one low-energy photon spectrometer (LEPS). The detectors were placed in

five rings at  $32^\circ$ ,  $57^\circ$ ,  $90^\circ$ ,  $123^\circ$ , and  $148^\circ$  with respect to the beam direction. The raw data were collected using a VME based data acquisition system [28], which were then written to a disk in a ROOT [29] Tree format. The energy and efficiency calibration were performed using a standard  $^{152}\text{Eu}$  source. The calibrated data were written into another ROOT Tree and various histograms were generated for further analysis. It may be noted that the two- and higher-fold coincidence data collected at the three beam energies were combined to determine the coincidence relationships between the  $\gamma$  rays, multiplicities of the transitions, and lifetime of isomeric states. In addition, single-fold data were also acquired to obtain the intensity information for the strong and noncontaminated  $\gamma$  rays.

The level scheme was constructed on the basis of coincidence relationships between the observed  $\gamma$  rays and the intensity measurements. In order to establish the coincidences between the  $\gamma$  rays, the transitions which were detected within 100 ns with respect to each other were used to construct symmetric two- and three-dimensional prompt histograms. Several *early-delayed*  $\gamma$ - $\gamma$  matrices within different time windows ( $\Delta T$ ) were generated to search for isomeric states. For such histograms, the transitions which precede (succeed) the coincident  $\gamma$  rays within a certain time interval ( $\Delta T$ ) are placed on the *early* (*delayed*) axis. In the present work, the half-life of the metastable state was extracted using the centroid-shift analysis. It may be noted the lifetimes greater than one-twentieth of the FWHM of prompt distribution can be extracted using the centroid-shift technique [30]. For the current detection setup, the FWHM was found to be around 50 ns for  $\gamma$  rays of  $\approx 500 \text{ keV}$  energy. For the centroid-shift analysis, histograms of time difference ( $\Delta T$ ) between the  $\gamma$  rays feeding and deexciting the state were generated.

The spin and parities of the states in the level scheme were assigned on the basis of the multiplicities of the  $\gamma$  rays. Since the intensities of the  $\gamma$  rays originating from the oriented nuclear states exhibit a particular angular dependence based on the multipole order of the transitions, the ratios of directional correlations of oriented states ( $R_{\text{DCO}}$ ) [31] were measured. An asymmetric  $\gamma$ - $\gamma$  matrix was generated with the transitions detected at  $32^\circ$  and  $148^\circ$  ( $\theta_1$ ) on the  $X$  axis and the coincident transitions detected at  $90^\circ$  ( $\theta_2$ ) on the  $Y$  axis. The  $R_{\text{DCO}}$  value for a given transition is defined as

$$R_{\text{DCO}}(\gamma_1) = \frac{I_{\gamma_1} \text{ at } \theta_1 | \text{gate on } \gamma_2 \text{ at } \theta_2}{I_{\gamma_1} \text{ at } \theta_2 | \text{gate on } \gamma_2 \text{ at } \theta_1}. \quad (1)$$

It was found that for a stretched quadrupole (dipole) gating transition, the  $R_{\text{DCO}}$  value for a quadrupole (dipole) transition is 1.0 (1.0), whereas the  $R_{\text{DCO}}$  value for a dipole (quadrupole)  $\gamma$  ray is 0.5 (2.0). Since the  $R_{\text{DCO}}$  values for the electric and magnetic transitions of a given multipole order are the same, polarization measurements were performed to ascertain the parities of the states.

The polarization asymmetry ( $\Delta_{\text{asym}}$ ) [32,33] for a transition of interest is defined as

$$\Delta_{\text{asym}} = \frac{a(E_\gamma)N_\perp - N_\parallel}{a(E_\gamma)N_\perp + N_\parallel}, \quad (2)$$

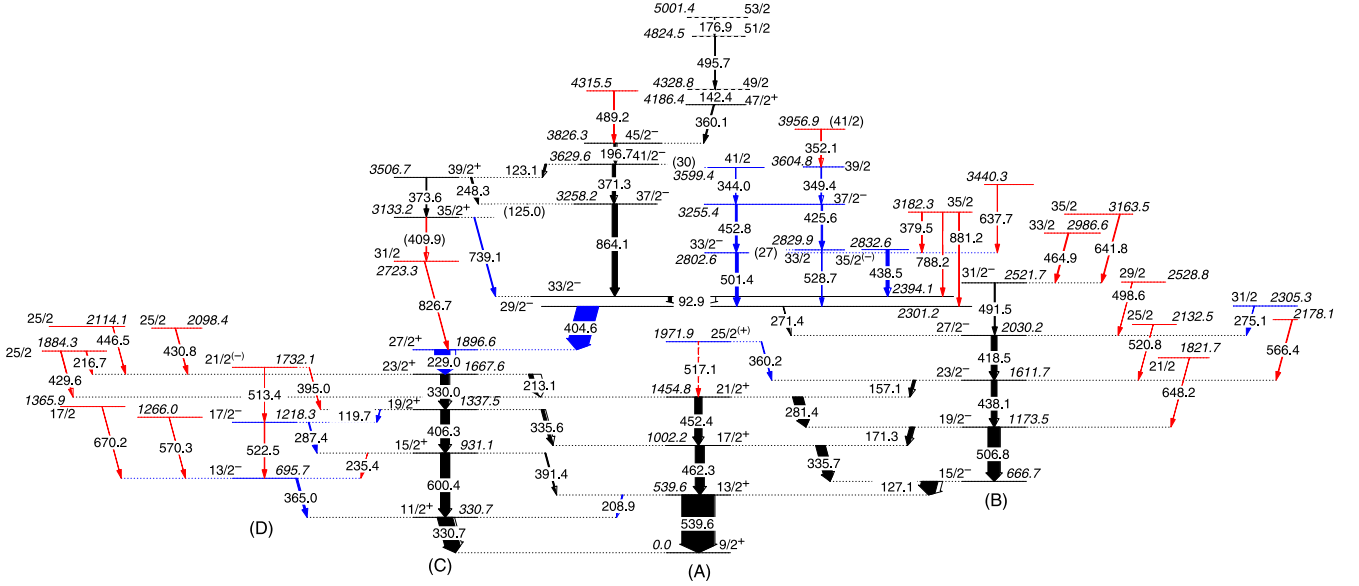


FIG. 1. The level scheme of  $^{217}\text{Ra}$  established in the present work. The widths of the closed and open areas of the arrows correspond to the intensity of the  $\gamma$  rays and conversion electrons, respectively. The newly identified  $\gamma$  rays and levels are presented in red color. The transitions whose placements were inconsistent in different studies [18,20,21] or uncertain in Ref. [38] and have been confirmed in the present work are shown in blue color. In addition, the earlier reported  $\gamma$  rays whose ordering has been changed are also shown in blue color.

where  $N_{\perp}$  ( $N_{\parallel}$ ) denotes the number of Compton-scattered  $\gamma$  rays detected in the direction perpendicular (parallel) with respect to the reaction plane.

The inherent geometrical asymmetry [ $a(E_{\gamma})$ ] in the polarization measurements is taken into account by determining the ratio of the parallel to perpendicular counts ( $\frac{N_{\parallel}}{N_{\perp}}$ ) for unpolarized gamma rays as a function of energy. For the present detection setup, the value of  $a(E_{\gamma})$  was found to be 1.02(2). The positive value of polarization asymmetry indicates the electric nature of the transition of interest, whereas the magnetic transitions have negative  $\Delta_{\text{asym}}$ . For the transitions where the measured  $\Delta_{\text{asym}}$  values are near zero and/or  $R_{\text{DCO}}$  measurements suggests mixed nature, information on the mixing of different multipoles is required. In order to determine the mixing ratios ( $\delta$ ), theoretical  $R_{\text{DCO}}$  and linear polarization ( $P$ ) values were compared with the experimental data points. The theoretical values of  $R_{\text{DCO}}$  and linear polarization ( $P$ ) were calculated using the formalism given in Refs. [34–36]. The value of spin alignment parameter was adopted to be 0.3 in the present calculations.

The linear polarization is related to the measured polarization asymmetry as

$$P = \frac{\Delta_{\text{asym}}}{Q(E_{\gamma})}. \quad (3)$$

The polarization sensitivity [ $Q(E_{\gamma})$ ] [33,36], which depends on the geometry of the polarimeter, varies as a function of energy as per the following relation:

$$Q(E_{\gamma}) = (CE_{\gamma} + D)Q_0(E_{\gamma}). \quad (4)$$

Here,  $Q_0(E_{\gamma})$  is the polarization sensitivity for a point absorber and scatterer and is defined as

$$Q_0(E_{\gamma}) = \frac{\alpha + 1}{\alpha^2 + \alpha + 1}, \quad (5)$$

with  $\alpha = E_{\gamma}/m_e c^2$ , where  $E_{\gamma}$  is energy of the incident  $\gamma$ -ray photon and  $m_e c^2$  is the rest-mass energy of the electron. The coefficients C and D for the polarization sensitivity were taken from Ref. [37].

### III. RESULTS

Figure 1 shows the level scheme of  $^{217}\text{Ra}$  established in the present study. Apart from a few modifications, the proposed level structure is found to be mostly consistent with that reported in Refs. [18,20]. In addition to the earlier reported transitions, around 20 new  $\gamma$  rays have been placed in the level scheme on the basis of coincidence relationships and intensity measurements. Also, the placements of several known transitions, which were found to be inconsistent in the earlier studies, have been confirmed in the present work. The multipolarities of the observed  $\gamma$  rays, wherever possible, were determined using the  $R_{\text{DCO}}$  and linear-polarization measurements. Table I lists the energies, relative intensities ( $I_{\gamma}$ ),  $R_{\text{DCO}}$ , and polarization values of the observed  $\gamma$  rays along with the spin-parities and excitation energies of the states. Furthermore, the established level scheme was investigated to search for isomers using *early-delayed*  $\gamma$ - $\gamma$  matrices. The present analysis does not indicate the presence of any longer-lived [ $\tau > 2.5$  ns] state other than the previously reported isomer with  $T_{1/2} = 4.62(6)$  ns at an excitation energy of 2.4 MeV [39]. The detailed results are discussed in the following subsections.

#### A. Revisiting the earlier reported level structures

It has been noted that out of the several transitions which were reported to directly populate the ground state in the recent  $\alpha$ -decay study [22], only 540- and 331-keV  $\gamma$  rays are

TABLE I. Table of  $\gamma$ -ray energies, level energies, spin-parity of the initial and final states, and relative  $\gamma$ -ray intensities of the transitions in  $^{217}\text{Ra}$ . The  $R_{\text{DCO}}$  values of the transitions in dipole and quadrupole gates are mentioned along with the linear polarization values and deduced multipolarity of the transitions. The reported errors in the  $\gamma$ -ray energies, relative  $\gamma$ -ray intensities, and  $R_{\text{DCO}}$  values include contribution from both the systematic and statistical uncertainties. The systematic uncertainty in  $I_\gamma$  is considered to be 5% of the relative  $\gamma$ -ray intensity.

$E_\gamma$ (keV)	$E_i$ (keV)	$I_i^\pi$	$I_f^\pi$ (keV)	$I_\gamma$	$R_{\text{DCO}}^Q$	$R_{\text{DCO}}^D$	$P$	Multipolarity
92.9(5)	2394.1(5)	33/2 <sup>-</sup>	29/2 <sup>-</sup>	2.1-3.9 <sup>a</sup>				
119.7(3)	1337.5(5)	19/2 <sup>+</sup>	17/2 <sup>-</sup>	1.3(3)	0.56(7)	1.16(16)		$D$
123.1(3)	3629.6(4)	41/2 <sup>-</sup>	39/2 <sup>+</sup>	4.6(2)	0.44(5)			$D$
(125.0) <sup>b</sup>	3258.2(1)	37/2 <sup>-</sup>	35/2 <sup>+</sup>	–				
127.1(1)	666.7(1)	15/2 <sup>-</sup>	13/2 <sup>+</sup>	49.9(25)	0.67(4)	1.20(7)		$E1^c$
142.4(4)	4328.8(4)	49/2	47/2 <sup>+</sup>	0.9(1)	0.64(3)			$D$
157.1(2)	1611.7(3)	23/2 <sup>-</sup>	21/2 <sup>+</sup>	7.4(4)	0.63(4)	1.15(8)		$E1^c$
171.3(2)	1173.5(2)	19/2 <sup>-</sup>	17/2 <sup>+</sup>	13.4(7)	0.60(3)	1.07(7)		$E1^c$
176.9(4)	5001.4(4)	53/2	51/2	0.3(1)	0.49(3)			$D$
196.7(2)	3826.3(2)	45/2 <sup>-</sup>	41/2 <sup>-</sup>	6.2(3)	1.11(9)	2.07(24)		$E2^c$
208.9(3)	539.6(3)	13/2 <sup>+</sup>	11/2 <sup>+</sup>	1.0(1)				
213.1(2)	1667.6(3)	23/2 <sup>+</sup>	21/2 <sup>+</sup>	13.0(7)	0.49(3)	1.00(6)		$D$
216.7(3)	1884.3(5)	25/2	23/2 <sup>+</sup>	2.0(1)	0.51(6)	0.94(19)		$D$
229.0(1)	1896.6(1)	27/2 <sup>+</sup>	23/2 <sup>+</sup>	47.8(24)	1.07(6)	1.94(12)	0.75(11)	$E2$
235.4(4)	931.1(5)	15/2 <sup>+</sup>	13/2 <sup>-</sup>	0.3(1)		0.99(22)		$D$
248.3(3)	3506.7(4)	39/2 <sup>+</sup>	37/2 <sup>-</sup>	4.5(2)	0.52(4)	0.98(11)		$D$
271.4(4)	2301.2(5)	29/2 <sup>-</sup>	27/2 <sup>-</sup>	0.9(1)	0.49(5)			$D$
275.1(3)	2305.3(3)	31/2	27/2 <sup>-</sup>	1.2(1)	1.00(12)			$Q$
281.4(1)	1454.8(4)	21/2 <sup>+</sup>	19/2 <sup>-</sup>	30.4(15)	0.55(3)	0.98(6)	0.49(8)	$E1$
287.4(3)	1218.3(4)	17/2 <sup>-</sup>	15/2 <sup>+</sup>	2.9(2)	0.53(6)	1.08(17)	0.54(11)	$E1$
330.0(1)	1667.6(3)	23/2 <sup>+</sup>	19/2 <sup>+</sup>	25.9(13)	1.06(6)		0.45(9)	$E2$
330.7(1)	330.7(1)	11/2 <sup>+</sup>	9/2 <sup>+</sup>	46.7(39)		1.45(13)	0.10(5)	$E2(+M1)^d$
335.6(2)	1337.5(5)	19/2 <sup>+</sup>	17/2 <sup>+</sup>	8.9(5)	0.54(4)		-0.10(3)	$M1$
335.7(1)	1002.2(3)	17/2 <sup>+</sup>	15/2 <sup>-</sup>	28.7(25)		1.00(7)	0.25(5)	$E1$
344.0(3)	3599.4(3)	41/2	37/2 <sup>-</sup>	1.4(1)	0.89(10)			$Q$
349.4(5)	3604.8(5)	39/2	37/2 <sup>-</sup>	1.3(2)	0.50(7)			$D$
352.1(4)	3956.9(4)	(41/2)	39/2	1.1(1)	0.75(14)			$D+Q$
360.1(3)	4186.4(3)	47/2 <sup>+</sup>	45/2 <sup>-</sup>	3.6(2)	0.54(4)	0.84(10)	0.37(7)	$E1$
360.2(5)	1971.9(5)	25/2 <sup>(+)</sup>	23/2 <sup>-</sup>	2.2(4)		0.85(9)		$D$
365.0(2)	695.7(2)	13/2 <sup>-</sup>	11/2 <sup>+</sup>	5.7(3)	0.53(8)		0.58(12)	$E1$
371.3(2)	3629.6(4)	41/2 <sup>-</sup>	37/2 <sup>-</sup>	9.4(5)	0.99(7)	1.91(19)	0.64(13)	$E2$
373.6(3)	3506.7(4)	39/2 <sup>+</sup>	35/2 <sup>+</sup>	2.4(1)	1.08(13)		0.56(13)	$E2$
379.5(4)	3182.3(7)	35/2	33/2 <sup>-</sup>	1.0(1)	0.52(7)			$D$
391.4(3)	931.1(5)	15/2 <sup>+</sup>	13/2 <sup>+</sup>	2.5(1)	0.73(6)			$D+Q$
395.0(4)	1732.1(6)	21/2 <sup>(-)</sup>	19/2 <sup>+</sup>	1.0(1)	0.47(5)			$D$
404.6(1)	2301.2(5)	29/2 <sup>-</sup>	27/2 <sup>+</sup>	63.5(32)	0.51(3)	1.02(6)	0.39(8)	$E1$
406.3(1)	1337.5(5)	19/2 <sup>+</sup>	15/2 <sup>+</sup>	25.7(57)	0.85(10)			$Q$
(409.9) <sup>b</sup>	3133.2(3)	35/2 <sup>+</sup>	31/2	–				
418.5(1)	2030.2(1)	27/2 <sup>-</sup>	23/2 <sup>-</sup>	17.0(9)	1.03(6)	1.81(15)	0.57(12)	$E2$
425.6(3)	3255.4(4)	37/2 <sup>-</sup>	33/2 <sup>-</sup>	4.1(2)	1.08(11)		0.64(14)	$E2$
429.6(5)	1884.3(5)	25/2	21/2 <sup>+</sup>	0.9(2)	0.86(11)			$Q$
430.8(5)	2098.4(5)	25/2	23/2 <sup>+</sup>	1.8(1)	0.46(5)			$D$
438.1(1)	1611.7(3)	23/2 <sup>-</sup>	19/2 <sup>-</sup>	16.8(13)	0.96(5)		0.53(12)	$E2$
438.5(2)	2832.6(2)	35/2 <sup>(-)</sup>	33/2 <sup>-</sup>	7.6(4)	0.59(4)	1.05(17)	0.03(3)	$(M1+E2)$
446.5(4)	2114.1(4)	25/2	23/2 <sup>+</sup>	1.0(1)	0.62(7)			$D$
452.4(1)	1454.8(4)	21/2 <sup>+</sup>	17/2 <sup>+</sup>	21.7(14)	0.99(8)		0.48(12)	$E2$
452.8(2)	3255.4(4)	37/2 <sup>-</sup>	33/2 <sup>-</sup>	5.3(3)	1.15(12)		0.51(13)	$E2$
462.3(1)	1002.2(3)	17/2 <sup>+</sup>	13/2 <sup>+</sup>	27.1(14)	1.04(8)	1.78(14)	0.65(15)	$E2$
464.9(3)	2986.6(3)	33/2	31/2 <sup>-</sup>	3.0(1)	0.49(5)	1.15(15)		$D$
489.2 (4)	4315.5(4)		45/2 <sup>-</sup>	0.7(1)				
491.5(3)	2521.7(3)	31/2 <sup>-</sup>	27/2 <sup>-</sup>	3.2(2)	1.08(8)		0.87(20)	$E2$
495.7(4)	4824.5(4)	51/2	49/2	0.4(1)	0.47(2)			$D$
498.6(4)	2528.8(4)	29/2	27/2 <sup>-</sup>	0.7(1)	0.48(6)			$D$
501.4(2)	2802.6(2)	33/2 <sup>-</sup>	29/2 <sup>-</sup>	8.4(4)	1.07(8)	2.12(22)	0.85(21)	$E2$



TABLE I. (Continued.)

$E_\gamma$ (keV)	$E_i$ (keV)	$I_i^\pi$	$I_f^\pi$	$I_\gamma$	$R_{\text{DCO}}^Q$	$R_{\text{DCO}}^D$	$P$	Multipolarity
506.8(1)	1173.5(2)	19/2 <sup>-</sup>	15/2 <sup>-</sup>	37.0(19)	1.04(6)	1.82(10)	0.69(17)	$E2$
513.4(5)	1732.1(6)	21/2 <sup>-</sup>	17/2 <sup>-</sup>	0.4(1)				
520.8(4)	2132.5(4)	25/2 <sup>-</sup>	23/2 <sup>-</sup>	0.7(1)	0.54(3)			$D$
522.5(3)	1218.3(4)	17/2 <sup>-</sup>	13/2 <sup>-</sup>	1.6(2)		2.06(25)		$Q$
528.7(4)	2829.9(4)	33/2	29/2 <sup>-</sup>	0.8(1)	0.86(13)			$Q$
539.6(1)	539.6(3)	13/2 <sup>+</sup>	9/2 <sup>+</sup>	100.0(52)	0.94(5)	1.86(1)	0.49(13)	$E2$
566.4(4)	2178.1(4)		23/2 <sup>-</sup>	2.1(1)				
570.3(4)	1266.0(4)		13/2 <sup>-</sup>	0.8(1)				
600.4(1)	931.1(5)	15/2 <sup>+</sup>	11/2 <sup>+</sup>	28.2(15)	0.90(5)		0.50(14)	$E2$
637.7(4)	3440.3(4)		33/2 <sup>-</sup>	0.9(1)				
641.8(3)	3163.5(3)	35/2	31/2 <sup>-</sup>	1.9(1)	0.89(5)			$Q$
648.2(4)	1821.7(4)	21/2	19/2 <sup>-</sup>	0.8(1)	0.54(5)			$D$
670.2(4)	1365.9(4)	17/2	13/2 <sup>-</sup>	1.0(1)		1.78(28)		$Q$
739.1(3)	3133.2(3)	35/2 <sup>+</sup>	33/2 <sup>-</sup>	3.0(1)	0.51(4)	0.82(9)	0.33(13)	$E1$
788.2(3)	3182.3(7)	35/2	33/2 <sup>-</sup>	1.1(1)	0.57(3)			$D$
826.7(3)	2723.3(3)	31/2	27/2 <sup>+</sup>	1.4(1)	0.81(10)			$Q$
864.1(1)	3258.2(1)	37/2 <sup>-</sup>	33/2 <sup>-</sup>	16.4(8)	1.04(6)	1.77(14)	0.93(41)	$E2$
881.2(4)	3182.3(7)	35/2	29/2 <sup>-</sup>	0.8(1)				

<sup>a</sup>Intensity range on the basis of total intensity balance at the 29/2<sup>-</sup> and 33/2<sup>-</sup> states assuming the  $E2$  multipolarity of the 93-keV transition.

<sup>b</sup> $\gamma$ -ray energy from the difference of corresponding level energies; centroid of the  $\gamma$  ray could not be unambiguously determined due to strong close lying transitions.

<sup>c</sup>From intensity balance considerations.

<sup>d</sup> $\delta = 6.1(3.6)$ ; large error in the  $\delta$  value can be attributed to the contribution of both systematic and statistical uncertainties in the  $R_{\text{DCO}}$  value.

observed in the present work and previous high-spin studies [18–21]. Figure 2 illustrates the  $\gamma$  rays in coincidence with the 540-keV transition. In addition to the several new transitions, most of the  $\gamma$  rays reported in the previous high-spin studies have been identified in this coincidence spectrum. Furthermore, it was observed that the deduced level structures from the present data are consistent with the reported ground-state “A” and negative-parity “B” sequences [18,20,21]. The level scheme of <sup>217</sup>Ra is particularly complex due to presence of several doublets in this nucleus. The 331-keV  $\gamma$  ray is

also a doublet and is observed to be in coincidence with its doublet counterpart 330-keV transition. Thus, to determine the multipolarity of the 331-keV transition, the  $\gamma$  rays in a parallel decay path with respect to the 330-keV  $\gamma$  ray were used as the gating transitions. The measured  $R_{\text{DCO}}$  and polarization values (see Table I) indicate the mixed dipole + quadrupole ( $E1 + M2$  or  $M1 + E2$ ) nature of the 331-keV transition. Therefore, to determine the true character of the transition, mixing ratio calculations were performed. As discussed in Sec. II, the mixing ratio for a transition of interest is determined by comparing the theoretical and experimental  $R_{\text{DCO}}$  and linear-polarization values. The theoretical values of the  $R_{\text{DCO}}$  and linear polarization were computed as a function of mixing ratio. Here, the theoretical contours were obtained by assuming both the positive and negative parity for the 331-keV state. The experimental point for the 331-keV  $\gamma$  ray is observed to be equidistant to both these contours (see Fig. 3). The comparison of the experimental data point with the contour for the  $M1 + E2$  multipolarity suggests a mixing ratio value of 6.1(36), which corresponds to  $\approx 97\%$   $E2$  component in the 331-keV transition. Another possibility is that the 331-keV  $\gamma$  ray is an  $E1 + M2$  transition with  $\approx 94\%$   $M2$  component [ $\delta = 3.8(8)$ ]. The Weisskopf estimate for an  $E1 + M2$  transition with dominant  $M2$  component suggests a half-life of  $\approx 75$  ns for the 331-keV state. However, the *early-delayed* analysis does not indicate the isomeric nature of the 331-keV state. Thus, the possibility of the 331-keV  $\gamma$  ray being an  $E1 + M2$  transition with a dominant  $M2$  component can be excluded. The present analysis suggests a mixed  $M1 + E2$  multipolarity for the 331-keV  $\gamma$  ray and, consequently, a spin-parity of 11/2<sup>+</sup> to the 331-keV state. The deduced spin-parity of the 331-keV state is consistent with the previous

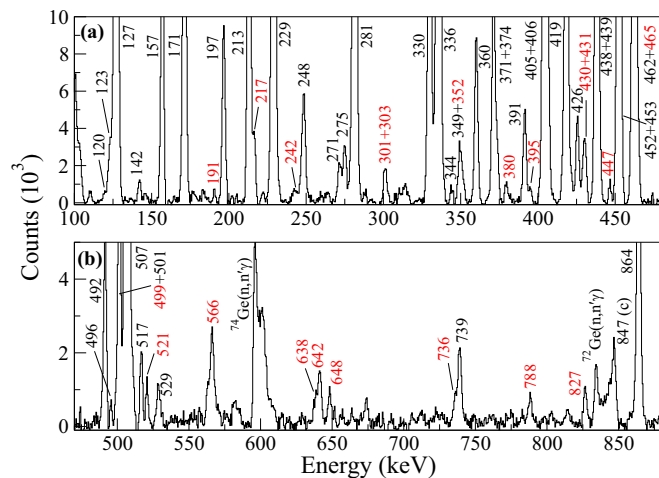


FIG. 2. Coincidence  $\gamma$ -ray spectra illustrating transitions in the gate of the 540-keV  $\gamma$  ray. The new transitions are labeled with red color. The contaminant line marked with (c) is from the reaction of the beam with the Fe target frame.

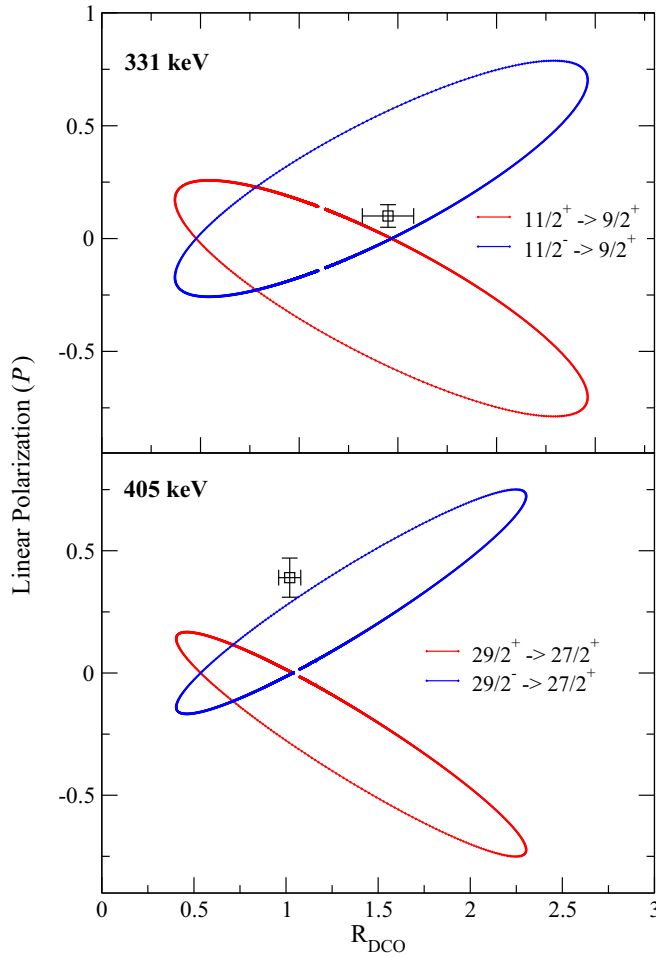


FIG. 3. Theoretical contours illustrating the calculated  $R_{\text{DCO}}$  and linear-polarization values ( $P$ ) as a function of mixing ratio ( $\delta$ ), along with the experimental data points, for the 331- and 405-keV transitions.

assignments from the  $\gamma$ -ray and conversion-electron spectroscopic studies [18–21]. In addition, Sheline *et al.* [40] had also suggested the same spin-parity for the 331-keV state based on the measured hindrance factors and the reflection-asymmetric model.

Similarly, the states up to  $23/2^+$  were established and the observed level structure was found to be in agreement with that reported in the earlier studies. The  $\gamma$ - $\gamma$  coincidence relationships suggest the presence of 229- and 405-keV transitions above the  $23/2^+$  state. However, their relative ordering was found to be inconsistent in Refs. [18,21]. Roy *et al.* [18] placed the 229-keV transition below the 405-keV  $\gamma$  ray on the basis of the presence of a prompt component in the time spectrum of the 229-keV transition. However, the ordering of these two transitions was reversed and a  $25/2^+$  state at 2.1 MeV energy was introduced in the level scheme proposed in Ref. [21]. In our work, a new 827-keV  $\gamma$  ray was identified in the gates of all the transitions below the 1668-keV state. A comparison of the gates of the 229- and 405-keV transitions, shown in Figs. 4(a) and 4(b), clearly reflects the coincidence between the 229- and 827-keV transitions. Furthermore, the

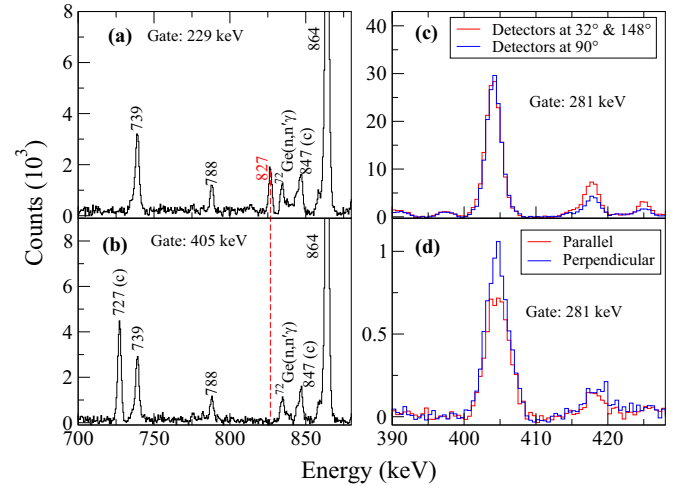


FIG. 4. Evidence for the placement and multipolarity of the 405-keV transition. Panels (a) and (b) illustrate the  $\gamma$  rays in coincidence with the 229- and 405-keV transitions, respectively. The presence/absence of the 827-keV  $\gamma$  ray is indicated. The contaminant peaks marked with (c) are from  $^{56}\text{Fe}$  and  $^{212}\text{Po}$ . Panel (c) shows a part of the representative gated  $\gamma$ -ray spectrum for the  $R_{\text{DCO}}$  measurements of the 405-keV  $\gamma$  ray, and panel (d) shows the counts in the parallel and perpendicular crystals of the  $90^\circ$  detectors reflecting the electric nature of the 405-keV transition.

placement of the 827-keV  $\gamma$  ray is supported by the presence of the 410- and 374-keV  $\gamma$  rays in the gate of the 827-keV transition. Thus, the relative ordering of the 229- and 405-keV transitions and a  $27/2^+$  state at 1897 keV were confirmed.

The  $R_{\text{DCO}}$  values for the 405-keV  $\gamma$  ray in the gate of stretched dipole and quadrupole transitions [see Table I and Fig. 4(c)] unambiguously suggest its  $\Delta I = 1$  character, which is also in agreement with the adopted [38] dipole nature of the transition based on the earlier angular distribution measurements [18,19]. Therefore, commensurate with the observed intensity of the 405-keV transition and the underlying reaction mechanism, we assign  $I = 29/2$  to the 2301-keV state. Furthermore, the linear-polarization measurements clearly indicate the electric nature of the transition. The deduced  $E1$  multipolarity of the 405-keV  $\gamma$  ray is in contrast to its previously assigned  $M1 + E2$  character with the dominant  $E2$  component [18]. Although the present data unambiguously suggest a  $I^\pi = 29/2^-$  to the 2301-keV state, the resulting variance with the previously reported assignments entailed us to further confirm the nature of the 405-keV transition using the mixing ratio calculations. The theoretical  $R_{\text{DCO}}$  and linear-polarization values were computed by assuming both the positive and negative parity of the 2301-keV state (see Fig. 3). It is apparent that the experimental data point is closer to the theoretical contour corresponding to the  $E1 + M2$  multipolarity and the point of intersection of the experimental data point on the contour suggests a near zero  $\delta$  value. This further corroborates the pure  $E1$  nature of the 405-keV  $\gamma$  ray and a spin-parity of  $29/2^-$  for the 2301-keV level.

Figures 5(a) and 5(b) illustrate the  $\gamma$  rays in the gate of 864- and 501-keV transitions, respectively. It is evident that both these  $\gamma$  rays are in coincidence with all the transitions below

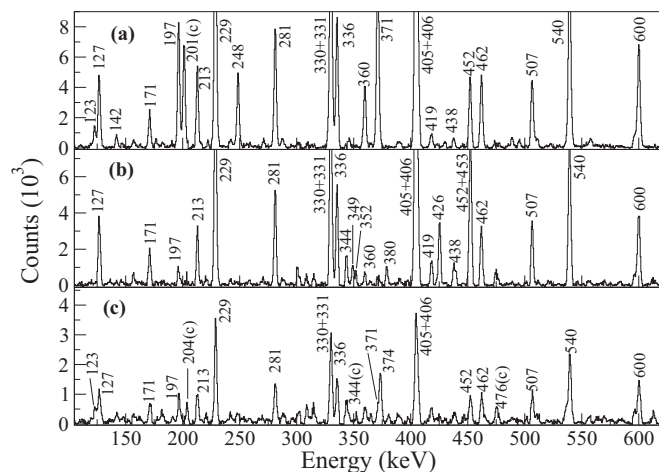


FIG. 5.  $\gamma$ -ray coincidence spectra illustrating transitions in the gate of the (a) 864-, (b) 501-, and (c) 739-keV transitions. The contaminant peaks marked with (c) are mainly from  $^{65}\text{Zn}$  and  $^{216}\text{Ra}$ .

the  $29/2^-$  state. Therefore, the 864- and 501-keV transitions can be placed directly above the  $29/2^-$  level. However, an isomeric state [ $T_{1/2} = 4.62(6)$  ns] with  $I^\pi = 33/2^+$  was identified at 2.4 MeV excitation energy and the 864-keV  $\gamma$  ray was placed above the isomer in the previous studies [18,20,38,39]. Also, it was reported that the  $33/2^+$  isomer deexcites via a 93-keV  $E2$  transition. Figure 6 shows the coincidence spectra observed in LEPS gated by the  $\gamma$  rays recorded in the clover detectors. The presence of the 93-keV  $\gamma$  ray in the gate of the 864-keV transition [Fig. 6(a)] is in agreement with the previous placement of these transitions. Furthermore, in the earlier work, the 93-keV  $\gamma$  ray was assigned  $E2$  character on the basis of conversion-coefficients measurements [18]. Considering the observed intensity (see Fig. 6) and the theoretical conversion-coefficients for the possible multipolarity ( $E1, M1, E2, M2, \dots$ ) of the 93-keV  $\gamma$  ray, the present data also supports its  $E2$  multipolarity. Since the present measure-

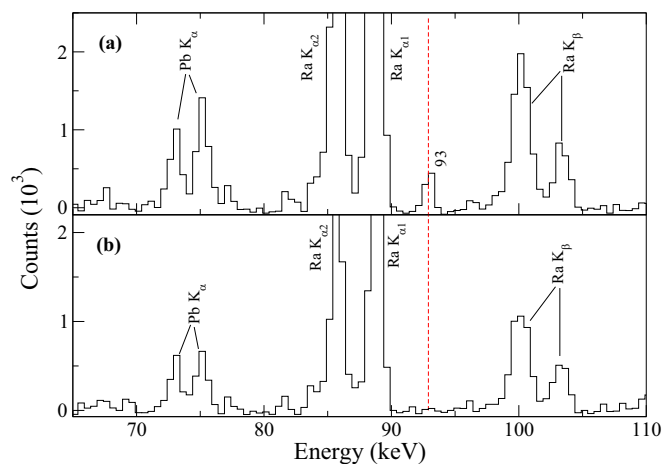


FIG. 6. Coincidence  $\gamma$ -ray spectra observed in the LEPS gated by the (a) 864- and (b) 501-keV  $\gamma$  rays recorded in the clover detectors.

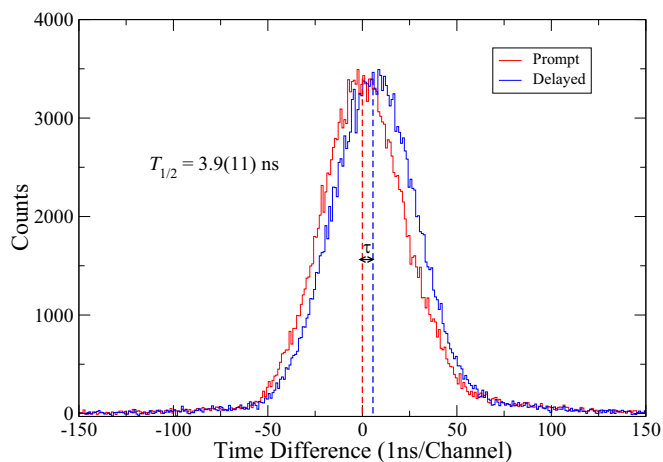


FIG. 7. Centroid-shift analysis to determine the cumulative half-life of the 2301- and 2394-keV states. The blue curve for the time difference between the 864- and 405-keV  $\gamma$  rays is compared with the time difference spectrum obtained using prompt transitions of similar energies. The difference between the centroids of the prompt and delayed distributions gives the cumulative mean life of the states.

ments have assigned the  $I^\pi = 29/2^-$  to the 2301-keV state, a spin-parity of  $33/2^-$  is deduced for the state at 2394 keV excitation energy.

Furthermore, the half-life of the 2394-keV state has been revisited using the centroid-shift analysis. In our work, the cumulative half-life of the 2301- and 2394-keV states was determined from the time difference between the 864- and 405-keV  $\gamma$  rays. The blue curve in Fig. 7 shows the time difference between the 864- and 405-keV  $\gamma$  rays which is compared with the time difference spectrum (in red color) of prompt transitions with similar energies. It is to be noted that the time difference spectra used for the comparison are generated after taking proper background subtraction into account. The cumulative half-life of the 2301- and 2394-keV states is deduced to be 3.9(11) ns which is found to be consistent with the adopted value of 4.62(6) ns for the 2394 keV state [38]. This suggests that the measured cumulative half-life is mainly due to the half-life of 2394-keV level. The error quoted in the half-life is obtained by adding the systematic and statistical errors in quadrature. The systematic error includes contributions from the discrete binning along the time axis and the uncertainty arising due to shift in the centroid of the prompt distribution of two similar energy transitions.

Furthermore, the placements of the 501- and 739-keV transitions were found to be at variance in Refs. [20,21]. The absence of the 93-keV transition in the gate of the 501-keV  $\gamma$  ray [Fig. 6(b)] confirms the placement of this transition as demonstrated in the present level scheme. Similar method could not be adopted to confirm the placement of the 739-keV  $\gamma$  ray owing to its weak intensity. However, the presence of the 123-, 197-, and 374-keV transitions in Fig. 5(c) confirms the placement of the 739-keV  $\gamma$  ray as shown in the Fig. 1. Similar analysis techniques were employed to confirm the remaining level structures reported in the earlier works.

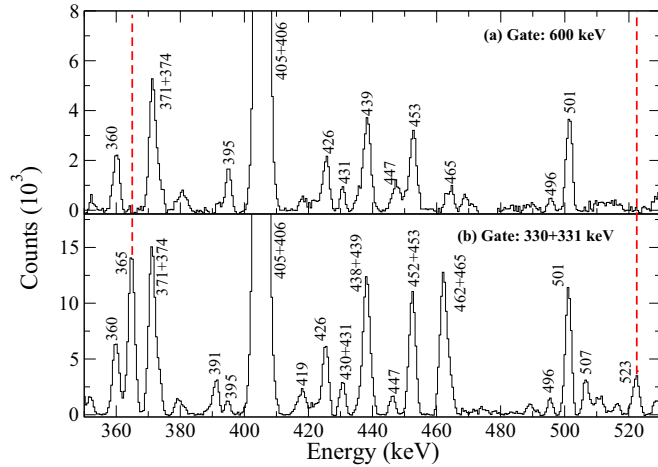


FIG. 8. A part of the coincidence  $\gamma$ -ray spectra in the gate of the (a) 600-keV transition and (b) 330-331 keV doublet. The presence/absence of the 365-keV transition is indicated.

### B. Evidence of parity doublets in $^{217}\text{Ra}$

Along with the two positive-parity and a negative-parity sequences below the isomer, a 1050-keV state was established on the basis of coincidence between 287- and 119-keV  $\gamma$  rays in the earlier studies [18,20,21]. In addition, a 365-keV transition was tentatively placed above the 1050-keV level in the work of Roy *et al.* [18]. However, in Ref. [21] the 365-keV transition was observed to deexcite the proposed  $13/2^+$  state at 696 keV energy. Figure 8 illustrates the coincident transitions in the gates of the 600- and 331-keV transitions. If the placement by Roy *et al.* [18] was correct, then the 600-keV transition should have been in the coincidence with the 365-keV  $\gamma$  ray. However, the absence of the 365-keV  $\gamma$  ray and a newly observed 523-keV transition in Fig. 8(a) clearly suggest that these transitions are parallel to the 600-keV  $\gamma$  ray.

Figure 9 shows the transitions in the gates of the 365- and 523-keV  $\gamma$  rays and confirms the coincidence relationship

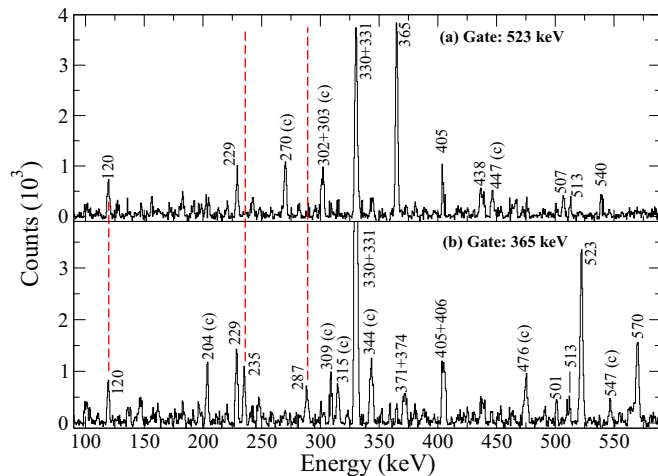


FIG. 9. A part of the coincidence  $\gamma$ -ray spectra illustrating transitions in the gate of the (a) 523- and (b) 365-keV  $\gamma$  rays provide evidence for reordering the 287- and 120-keV transitions. The contaminant peaks marked with (c) are mainly from  $^{214}\text{Rn}$  and  $^{216}\text{Ra}$ .

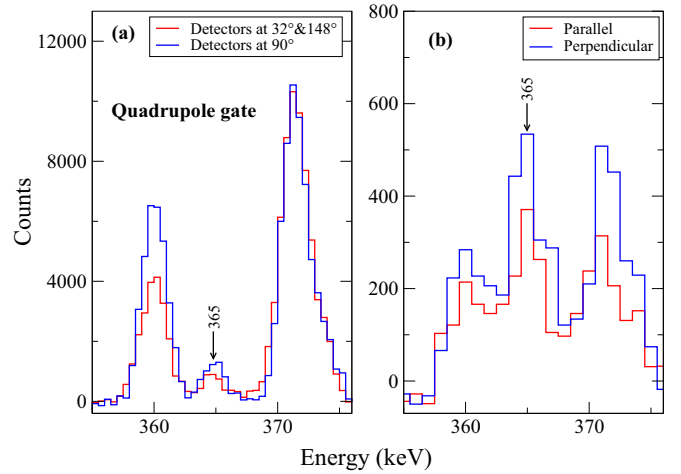


FIG. 10. Representative spectra corresponding to the (a)  $R_{\text{DCO}}$  and (b) polarization measurements of 365-keV transition.

between these transitions. The placement of the 365- and 523-keV  $\gamma$  rays, as indicated in the Fig. 1, is based on the observed coincidences and intensity considerations. Furthermore, the absence of the 287-keV transition in Fig. 9(a) indicates that the ordering of the 287- and 120-keV transitions as suggested in Refs. [18,20,21] should be reversed. Similar coincidence relationships were utilized to secure the placement of newly identified 395- and 513-keV transitions which, in turn, establishes a state at 1732 keV excitation energy.

Furthermore, the  $R_{\text{DCO}}$  and linear-polarization values of the observed transitions were utilized to assign the spin-parities to the newly established states. In the gate of the 229-keV  $\gamma$  ray, which is a stretched  $\Delta I = 2$  transition, the  $R_{\text{DCO}}$  value for the 365-keV transition is found to be 0.53(8) (see Fig. 10(a) and Table I). This suggests the dipole character of the 365-keV transition. Figure 10(b) illustrates a part of the representative spectra for the polarization measurements and higher counts in the spectrum corresponding to the perpendicular scatterings with respect to the reaction plane clearly indicates the electric nature of the 365-keV  $\gamma$  ray. Thus, a spin-parity of  $13/2^-$  is assigned to the 696-keV state. Furthermore, the measured DCO ratios for the 287- and 523-keV transitions and polarization values for the 287-keV  $\gamma$  ray suggest the spin-parity of  $17/2^-$  for the 1218-keV level. Similarly, the  $R_{\text{DCO}}$  measurements for the 395-keV transition suggests  $I = 21/2$  for the 1732-keV state. However, the electric/magnetic character of the transitions depopulating the 1732-keV state could not be determined due to poor statistics. The negative parity of the  $21/2$  state is tentatively assigned on the basis of striking similarity in the observed low-lying structures of  $^{217}\text{Ra}$  and  $^{219}\text{Th}$  [13]. As discussed in Sec. I, parity-doublet structures are a signature of octupole correlations in odd- $A$  and odd-odd nuclei. Thus, the newly established negative-parity sequence provides an experimental evidence of parity doublets in  $^{217}\text{Ra}$  and reflects the expected similarity in the structures of the transitional  $N = 129$  isotones. Similar analysis techniques were employed to determine the placement and multipolarity of the remaining newly identified  $\gamma$  rays, wherever possible.



The present data also suggest a few unobserved transitions in the level scheme based on the  $\gamma$ - $\gamma$  coincidences. The coincidence relationships of the 501- and 529-keV  $\gamma$  rays with the 426-keV and other higher-lying transitions indicate the presence of an unobserved 27-keV transition between the 2830- and 2803-keV states. Similarly, the coincidences of the 197- and 360-keV transitions with the  $\gamma$  rays below the 3599-keV state suggest an unobserved 30-keV transition between the  $41/2^-$  state and  $41/2$  state at 3599 keV energy. Also, the coincidence relationship between the 739- and 371-keV  $\gamma$  rays requires a 125-keV transition, which has been reported in earlier studies [18,20], between the 3258- and 3133-keV states. The centroid and intensity information of the 125-keV transition could not be determined due to the presence of stronger close-lying 123- and 127-keV transitions. Moreover, the 465- and 642-keV transitions are observed to be in coincidence with the 405-keV  $\gamma$  ray and the transitions of sequence “C”. This suggests that the  $31/2^-$  state deexcites to the low-lying  $29/2^-$  and/or  $33/2^-$  states, via weak unobserved transitions.

Several new transitions (viz. 191-, 242-, 301-, 303-, 736-, 859-, 968-keV), which were assigned to  $^{217}\text{Ra}$  in the present study, could not be unambiguously placed in the level scheme. These transitions are observed to be in coincidence with all the  $\gamma$  rays below the  $29/2^-$  state. However, due to their weak intensities and/or the lack of firm coincidence relationships with the other known  $\gamma$  rays above the  $29/2^-$  state, the placement of these transitions could not be ascertained. Furthermore, the present data also suggest a doublet character of the 517-keV transition. One component of the 517-keV doublet is placed between the  $25/2^{(+)}$  and  $21/2^+$  states, whereas the coincidence relationships suggest the placement of the second 517-keV  $\gamma$  ray above the  $29/2^-$  level. In Ref. [20], the 517-keV transition was reported to deexcite the 3259-keV state and populate the 2301-keV level via a 440-keV transition. However, due to absence of a transition at 440 keV and other suitable coincidences of the 517-keV transition above the  $29/2^-$  level, the placement of the second 517-keV  $\gamma$  ray remains inconclusive in the present work, similar to the several transitions mentioned above.

### C. Intensity measurements

The relative intensities of the observed  $\gamma$  rays were determined using the data collected at 72 MeV beam energy. The data acquired in the single fold were utilized to obtain the intensity information for the strong, noncontaminated (viz. 540-, 229-, 213-, and 462-keV)  $\gamma$  rays. The intensities of all the transitions observed in  $^{217}\text{Ra}$  were normalized with respect to that of the 540-keV  $\gamma$  ray, which is assumed to be 100. Due to the presence of several doublets in the level scheme, suitable approaches were employed to determine the relative intensities of the observed  $\gamma$  rays. The 331-keV transition, which directly feeds the ground state, has also been identified as a doublet. Therefore, the intensities of the transitions parallel to the 330-keV ( $23/2^+ \rightarrow 19/2^+$ )  $\gamma$  ray were obtained in the efficiency corrected summed gate of 540- and 331-keV transitions and normalized with respect to the relative intensity of the 213-keV  $\gamma$  ray. A few transitions, which are in a

parallel decay path with respect to the 330-keV  $\gamma$  ray, such as 452-, 438-, and 360-keV, were also identified as doublets. Since the doublet counterparts of these transitions are placed above the isomer and are in coincidence with both the 330- and 331-keV  $\gamma$  rays, their intensities could not be determined in the summed gate of the 540- and 331-keV transitions.

In order to determine the intensities of transitions which are in coincidence with both the  $\gamma$  rays of 330–331 keV doublet, it was important to extract the individual intensity of the 331-keV transition. It may be noted that the 540-keV transition is in coincidence with only the 330-keV  $\gamma$  ray. Therefore, the intensity of the 330-keV transition was determined in the gate of 540-keV  $\gamma$  ray and normalized with respect to the relative intensity of 462-keV  $\gamma$  ray. The relative intensity thus obtained was further corrected for the decay branch of the  $19/2^+$  state using the relative intensity of the 395-keV transition. The total intensity of 330–331 keV doublet was determined from the single fold data. Thus, the relative intensity of the 331-keV transition was deduced after subtracting the contribution of the 330-keV  $\gamma$  ray from the summed total relative intensity of the doublet line. Once the relative intensity of the 331-keV  $\gamma$  ray was known, the intensities of the transitions above the  $23/2^+$  state were extracted from the efficiency and branching corrected 540-keV gate and normalized with respect to the intensity of the 462-keV  $\gamma$  ray. It may be noted that the relative intensities of the noncontaminated transitions could also be determined in the efficiency corrected summed gate of the 540-, 209-, 365-, and 600-keV  $\gamma$  rays and normalized with respect to that of the 229-keV transition. It was observed that the intensities of the noncontaminated transitions obtained from the above two approaches were consistent with each other.

In order to resolve the doublets, wherever possible, appropriate methods were employed. For example, the total intensity of the 452-453 keV doublet was determined using the singles data. The gate of the 281-keV transition, which is in a parallel decay path with respect to the 452-keV ( $21/2^+ \rightarrow 17/2^+$ )  $\gamma$  ray, was utilized to find the relative intensity of the 453-keV transition lying above the isomer. The deduced intensity was then normalized with respect to the relative intensity of the 501-keV transition. Further, the intensity of the 452-keV  $\gamma$  ray was extracted by subtracting the contribution of the 453-keV transition from the doublet line. Similarly, suitable coincidence relationships were utilized to determine the intensities of the transitions in the remaining doublets.

The above discussion includes the information on the intensity measurements of all transitions except for the  $\gamma$  rays of the newly established negative-parity sequence. The branching ratio of the 120- and 406-keV  $\gamma$  rays, measured in the gate of the 395-keV transition, was utilized to deduce the relative intensity of the 120-keV transition. Furthermore, the intensity of the 287-keV transition was obtained in the 600-keV gate and normalized with respect to the relative intensity of the 406-keV transition. The branching of the 287- and 523-keV  $\gamma$  rays in the 120-keV gate was determined to extract the intensity of the 523-keV transition. The relative intensities of the 235-, 570- and 670-keV transitions were extracted in the gate of the 365-keV  $\gamma$  ray and were normalized with respect to that of the 523-keV transition. Finally, the intensity of the

365-keV  $\gamma$  ray was obtained in the gate of the 330-331 keV doublet and the relative intensity of the 523-keV  $\gamma$  ray was used for normalization.

#### IV. DISCUSSION

As discussed in Sec. I,  $^{217}\text{Ra}$  with  $Z = 88$  and  $N = 129$  lies in the transitional region between the spherical and static octupole-deformed nuclei. The earlier reported low-lying sequences starting with  $9/2^+$ ,  $11/2^+$ , and  $15/2^-$  states were qualitatively understood in terms of mainly the shell-model configurations viz.  $\nu g_{9/2}^3$ ,  $\nu g_{9/2}^2 i_{11/2}$ , and  $\nu g_{9/2}^2 j_{15/2}$ , respectively [18]. Although these sequences were reported to terminate at the spins predicted by the above mentioned configurations, the almost constant level spacings observed in the ground-state and negative-parity sequences along with the strong  $E1$  connecting transitions reflected the contribution of collective degrees of freedom in this nucleus. In the present work, a new negative-parity sequence has been established along with the above mentioned three sequences. The addition of this newly established negative-parity sequence hints at the parity-doublet structures in  $^{217}\text{Ra}$ , which are expected in an odd- $A$  nucleus displaying octupole correlations. Furthermore, the two alternating-parity sequences established in  $^{217}\text{Ra}$  are characterized by the simplex quantum number ( $s$ ) [41]. It is known that for even- $A$  nuclei the sequences  $0^\pm$ ,  $1^\mp$ ,  $2^\pm$ ,  $3^\mp$ ,  $4^\pm$ , ... are associated with the  $s = \pm 1$  quantum number, respectively. In the case of odd- $A$  nuclei,  $s = \pm i$  is assigned to the  $1/2^\pm$ ,  $3/2^\mp$ ,  $5/2^\pm$ ,  $7/2^\mp$ ,  $9/2^\pm$ , ... sequences, respectively.

The properties of the observed simplex bands in  $^{217}\text{Ra}$  are compared with those of the similar bands in the neighboring nuclei. The energy splitting, which is defined as the difference between the excitation energies of the states of same spin but opposite parity/simplex, indicates the strength of octupole correlations in a given nucleus. Ideally, a near zero splitting is expected in the nuclei with static octupole deformation. In the case of  $^{223}\text{Th}$  ( $Z = 90$  and  $N = 133$ ), an average energy splitting of  $\approx 30$  keV is observed which suggests a stable deformation in this nucleus [42]. However, the large average energy splitting ( $\approx 190$  keV) in  $^{217}\text{Ra}$  [see Fig. 11(a)] indicates that the static octupole deformation has not set in this transitional nucleus. Figure 12 illustrates the variation of the initial spin with rotational frequency for the  $s = +i(+1)$  band in  $^{217}\text{Ra}$  and neighboring nuclei. This relation generally indicates the extent of rotation-like behavior in a nucleus. It may be noted that the  $I(\omega)$  pattern for  $^{217}\text{Ra}$  is consistent with the almost constant level spacings in the ground-state  $E2$  sequence. Also, the similarity in the  $I(\omega)$  trend observed in all the  $N = 129$  isotones suggests that the addition/removal of a proton in the  $h_{9/2}$  orbital does not significantly influence the dependence of excitation energy on the spin. Furthermore, the comparison of the observed  $I(\omega)$  for the  $N = 129$  and  $N = 131$  isotones clearly suggests that the excitation energy of the states better resembles with the behavior expected for typical rotational bands with the increase in neutron number. This, in turn, indicates that the quadrupole deformation in this region is more sensitive to the number of valence neutrons outside the shell closure.

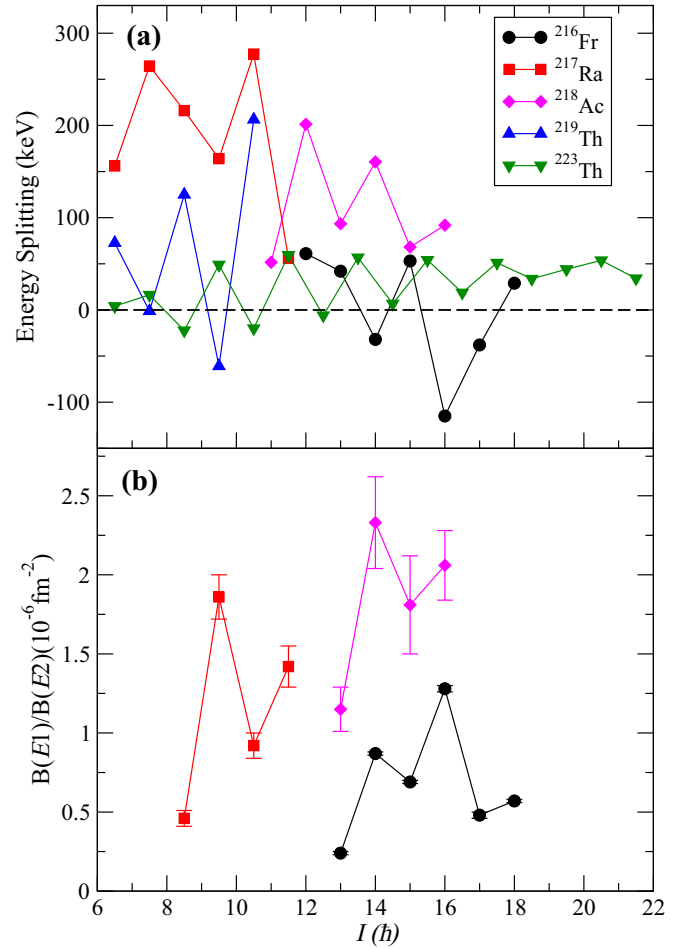


FIG. 11. Comparison of the (a) energy splitting [ $E(s=-i/-1) - E(s=+i/+1)$ ] and (b)  $B(E1)/B(E2)$  ratios versus initial spin for the transitions of  $s = +i$  band in  $^{217}\text{Ra}$  with  $N = 129$  isotones ( $^{216}\text{Fr}$ ,  $^{218}\text{Ac}$ ,  $^{219}\text{Th}$ ). The data are taken from Refs. [13,25,26] and the present work.

Furthermore, the experimental  $B(E1)/B(E2)$  ratios were extracted using the measured  $\gamma$ -ray intensities. The deduced ratios are of the order of  $\approx 10^{-6} \text{ fm}^{-2}$  which are consistent with the benchmark values if octupole correlations are present in a nucleus. It is apparent from Fig. 11(b) that the  $B(E1)/B(E2)$  ratios for the negative-parity states lie higher than that for the positive-parity states in  $^{217}\text{Ra}$ , whereas the converse is true for the odd-odd ( $^{216}\text{Fr}$ ,  $^{218}\text{Ac}$ ) nuclei. In a stable octupole deformed nucleus, the strengths of the electric dipole transitions [ $I^\pm \rightarrow (I-1)^\mp$ ] should be independent of the parity of the initial state [14]. However, the  $E1$  transitions originating from the positive parity states are forbidden in the framework of a pure vibrational model [14,26]. As the unpaired proton and neutron occupies the  $h_{9/2}$  and  $g_{9/2}$  orbitals, respectively, the higher ratios for the negative (positive) parity state in odd- $A$  (odd-odd) nuclei are consistent with an intermediate behavior between the extremes discussed above. It is important to note that the staggering in the  $B(E1)/B(E2)$  ratios can only be related to the staggering in the  $B(E1)$  values if a constant quadrupole deformation is assumed. Therefore, to understand the actual variation of reduced transition

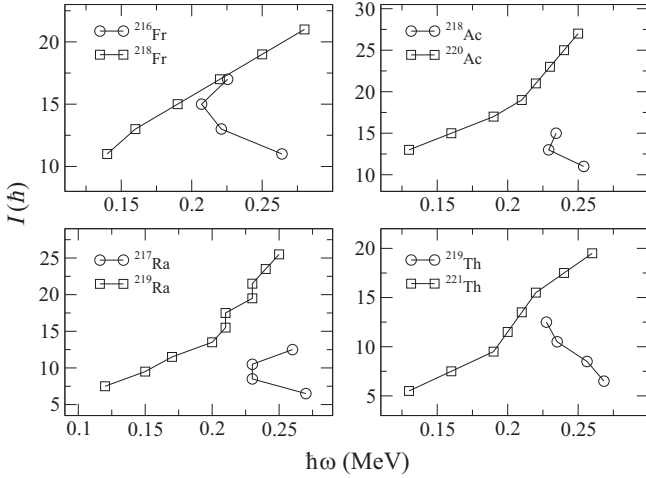


FIG. 12. Systematics of the spin ( $I$ ) versus rotational frequency  $[\hbar\omega(I) = [E(I) - E(I - 2)]/2]$  for the lowest lying sequence of the  $s = +i/+1$  bands in the  $N = 129$  and  $131$  isotones with  $87 \leq Z \leq 90$  [13,25,26,43–46].

probabilities and their corresponding ratios with angular momentum, measurements for determining the lifetimes of the states are required.

From the above discussion on the energy splitting,  $I(\omega)$ , and  $B(E1)/B(E2)$  ratios, it is evident that the quadrupole and octupole deformations are not fully developed in the  $^{217}\text{Ra}$ . However, the newly established parity-doublet structures are a clear indication of octupole correlations in this nucleus. Therefore, for a more quantitative understanding, theoretical calculations including octupole degrees of freedom were performed using reflection-asymmetric triaxial particle rotor model (RAT-PRM) [47]. Recently, RAT-PRM has also been employed to investigate a possibility of coexistence of nuclear chirality and octupole correlations in the form of multiple chiral bands [48–51].

The quadrupole and octupole deformation parameters are taken as input in the RAT-PRM calculations. In the case of  $^{217}\text{Ra}$ , the corresponding  $\beta_2 = 0.05$  and  $\beta_3 = 0.08$  were adopted from the Ref. [52]. With these deformation parameters, the reflection-asymmetric Hamiltonian was solved by expanding the wave function in harmonic oscillator basis [53]. The single-particle space available to the odd nucleon was truncated to include six levels, each above and below the Fermi surface. The pairing correlation was taken into account by an empirical pairing gap formula  $\Delta = 12/\sqrt{A}$  MeV. For the core part, a spin-dependent moment of inertia  $\mathcal{J}_0 = (3.1 + 1.24I) \hbar^2/\text{MeV}$  and the core parity-splitting parameter  $E(0^-) = 2.0$  MeV were used. Also, the Coriolis attenuation parameters ( $\xi^\pm$ ) for the positive and negative parity states were taken to be 0.7 and 1, respectively. In addition, the electromagnetic transition probabilities were calculated by assuming intrinsic dipole moment and quadrupole moments  $0.0006 * AZe\beta_2\beta_3$  and  $(3/\sqrt{5\pi})R_0^2Z\beta_2$ , respectively [54,55].

The energies calculated from the RAT-PRM calculations for the  $s = +i$  and  $s = -i$  bands are compared with the experimental excitation energies in Fig. 13. The calculated energies

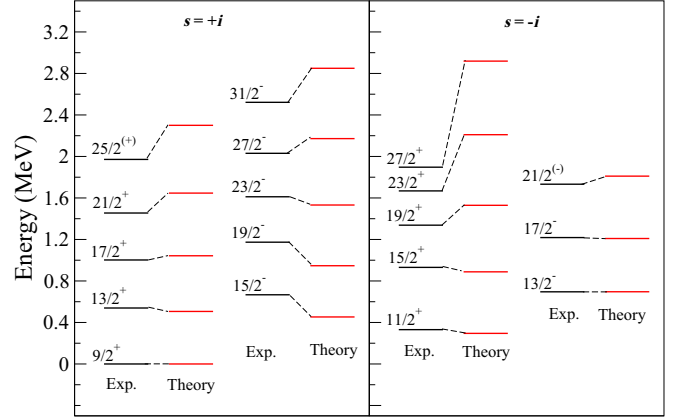


FIG. 13. Comparison of the experimental results with the predictions of the RAT-PRM calculations for the simplex bands in  $^{217}\text{Ra}$ .

for the positive- and negative-parity states are shifted to coincide with the experimental energy of  $9/2^+$  and  $13/2^-$  states, respectively. It is observed that the results of the calculations are in good agreement with the experimental energies up to  $I^\pi = 21/2^+$  for the positive-parity states and  $I^\pi = 27/2^-$  for the negative-parity states. The deviation between the calculated and experimental energies at higher angular momentum may be attributed to the fact that the vibrational effects could not be included in the present RAT-PRM calculations.

Since  $^{217}\text{Ra}$  is an odd- $N$  nucleus, the main components of the intrinsic wave functions of the states are dominated by the neutron configurations. As the RAT-PRM calculations include a finite  $\beta_3$ , the intrinsic parity is not a good quantum number and the neutron  $g_{9/2}$  and  $j_{15/2}$  orbitals mix with each other. The main components of the intrinsic wave functions were expanded in the strong-coupled basis  $|IMK\rangle \chi^\nu$  (denoted as  $|K, \nu\rangle$  for short), where  $|IMK\rangle$  is the Wigner function with  $I$ ,  $M$ , and  $K$  denoting the quantum numbers of the total angular momentum and its projections along the third axis in the laboratory frame and intrinsic frame, respectively, and  $\chi^\nu$  represents the intrinsic wave function of the neutron single-particle level  $|\nu\rangle$ . The neutron single-particle levels  $|1\rangle$ ,  $|2\rangle$ ,  $|3\rangle$ ,  $|4\rangle$  and  $|5\rangle$  predominately involve  $g_{9/2}$  orbital with different  $\Omega = 9/2, 7/2, 5/2, 3/2$ , and  $1/2$ , respectively (see Table II).

Figures 14 and 15 illustrate the main components of the wave functions for the positive- and negative-parity states of the  $s = \pm i$  bands, respectively. It may be noted that the components corresponding to different neutron single-particle levels strongly mix with each other. Furthermore, it is known

TABLE II. The main components  $l_{j\Omega}$  of the neutron single-particle levels  $|\nu\rangle$  with  $\nu = 1, 2, 3, 4$ , and  $5$ .

$ \nu\rangle$	Main components of the neutron single-particle levels
1)	$0.948 g_{9/2,9/2} + 0.022 h_{11/2,9/2} + 0.022 j_{15/2,9/2} + \dots$
2)	$0.902 g_{9/2,7/2} + 0.055 j_{15/2,7/2} + 0.018 f_{7/2,7/2} + \dots$
3)	$0.878 g_{9/2,5/2} + 0.076 j_{15/2,5/2} + 0.010 i_{13/2,5/2} + \dots$
4)	$0.810 g_{9/2,3/2} + 0.087 j_{15/2,3/2} + 0.031 p_{3/2,3/2} + \dots$
5)	$0.755 g_{9/2,1/2} + 0.093 j_{15/2,1/2} + 0.067 p_{3/2,1/2} + \dots$

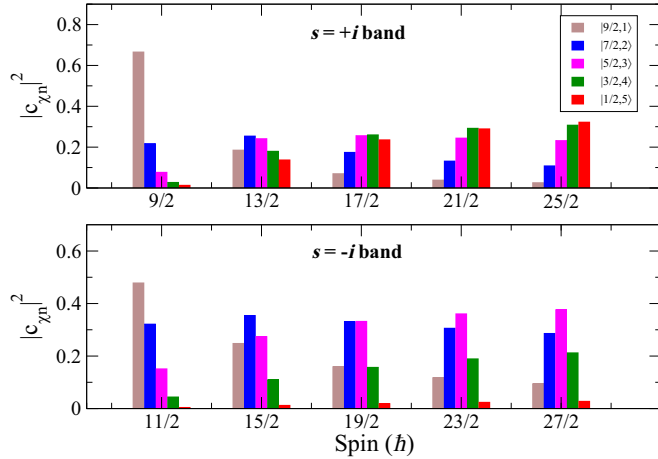


FIG. 14. The probability amplitudes of the main components of the intrinsic wave functions for the positive-parity states of the  $s = \pm i$  bands in  $^{217}\text{Ra}$ .

that the strong Coriolis effects for the low  $\Omega$  orbitals result in lowering the energies of the states which have dominant contribution from such orbitals [56]. A comparison of the relative contribution of the single-particle levels with different  $\Omega$  values in the wave functions of the positive-parity states (see Fig. 14) suggests that the states in  $s = +i$  band are more favored than the corresponding states in  $s = -i$  band. This is in agreement with the experimental observations and is reflected in the staggering parameters  $[S(I) = [E(I) - E(I - 1)]/2I]$  of the positive-parity states in Fig. 16(a). Similarly, it is observed that the single-particle level |5> ( $\Omega = 1/2$ ) significantly contributes to the wave function of all the negative-parity states of  $s = +i$  band. However, the negative-parity states of the  $s = -i$  band have a dominant contribution from the  $\Omega = 5/2$  orbital. The effect of the Coriolis interactions suggests the lowering of energies for the states of the  $s = +i$  band, which also agrees with the observed results. The large energy staggering for the negative-parity states is in agreement with the comparatively weak intensity of the newly identified negative-parity sequence.

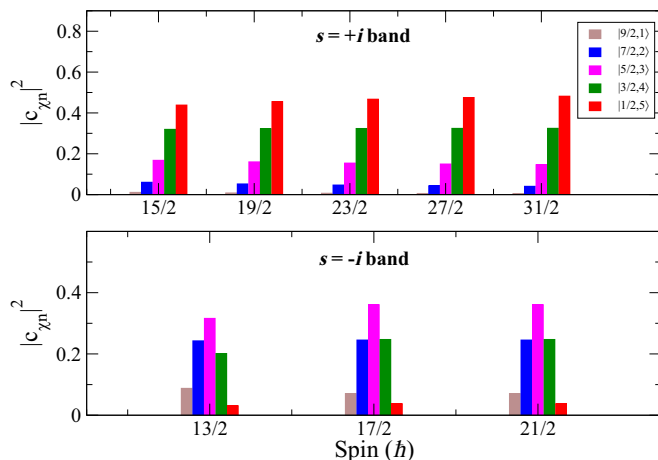


FIG. 15. Same as Fig. 14, but for the negative-parity states.

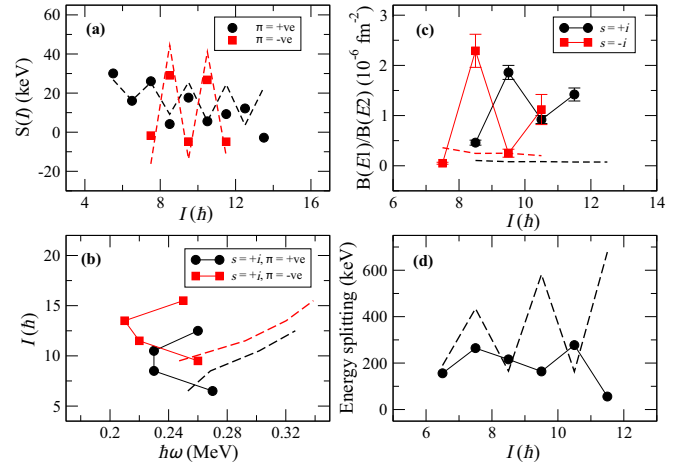


FIG. 16. Comparison of the calculated (a) energy staggering parameters  $[S(I)]$ , (b)  $I$  vs  $\hbar\omega$ , (c)  $B(E1)/B(E2)$  ratios, and (d) energy splitting with the experimental results for the simplex bands in  $^{217}\text{Ra}$ . The results of the calculations are shown with the dashed lines of the same color.

Figure 16 shows a comparison of the observed features of the simplex partner bands in  $^{217}\text{Ra}$  with the results of the RAT-PRM calculations (dashed lines). It is evident from Fig. 16(a) that the RAT-PRM calculations are able to reproduce the phase of staggering for both the positive- and negative-parity states. Also, the calculated values are in excellent agreement with the observed staggering for the negative-parity states, whereas a good agreement is observed for the positive-parity states in the spin range  $11/2 \hbar \leq I \leq 21/2 \hbar$ . Figure 16(b) illustrates the spin ( $I$ ) versus rotational frequency ( $\hbar\omega$ ) for the  $s = +i$  band. The experimental  $I(\omega)$  relation for both the positive- and negative-parity states reflects the almost constant level spacing in these sequences. However, the calculated values exhibit a gradually increasing spacing between the states of the bands. Figure 16(c) shows the variation of the  $B(E1)/B(E2)$  ratios with spin for both the  $s = \pm i$  bands and the calculated results are shown for the comparison. It may be noted that the calculated values are almost constant and significantly underestimated as compared to the observed ratios for both the simplex bands. The absence of spin-dependent staggering in the calculated ratios may be due to the fact that the vibrational effects could not be taken into account in the calculations. Furthermore, the calculated and experimental energy splittings between the states of simplex bands are compared in Fig. 16(d). It is observed that the calculated energy splittings for the parity doublets with  $I = 19/2 \hbar$  and  $23/2 \hbar$  deviate considerably from the measured ones. This is in accordance with the large difference in the calculated excitation energies for the corresponding states of the  $s = \pm i$  bands (see Fig. 13). Finally, the comparison of the experimental results with the RAT-PRM predictions further corroborates the fact that the quadrupole and octupole deformation are not fully developed in  $^{217}\text{Ra}$  and this transitional nucleus lies between the extremes of spherical and pear shaped nuclei. Also, further improvements to include the vibrational effects in the calculations are needed.



It is interesting to note that the simplex bands observed in  $^{217}\text{Ra}$  may also be qualitatively interpreted in terms of the weak coupling of the odd nucleon to the neighboring even-even core nuclei. As discussed earlier, the observed level structures in  $^{216}\text{Ra}$  and  $^{218}\text{Ra}$  exhibit the dominance of single-particle and octupole degrees of freedom, respectively [15,17]. The level spacings in the ground-state positive-parity sequence “A” of  $^{217}\text{Ra}$  exhibit a vibrational like structure which is similar to that observed in  $^{218}\text{Ra}$ , whereas the decreasing level spacings in the second positive-parity sequence “C” suggests the coupling of the odd neutron in the  $i_{11/2}$  orbital to the low-lying ( $0^+-8^+$ ) states of  $^{216}\text{Ra}$ . The corresponding negative-parity sequences may be understood as arising from the coupling of an octupole phonon to the states of these positive-parity sequences. Similar interpretation has also been employed in understanding the observed structures in  $^{219}\text{Th}$  nucleus [13].

Furthermore, it has been pointed out that the negative-parity states in the even-even Ra isotopes ( $N \geq 126$ ) reflect how the structure evolves from spherical to octupole deformed regime [58]. The lowest negative-parity state ( $I^\pi = 11^-$ ) in the lighter Ra isotopes (viz.  $^{214}\text{Ra}$  and  $^{216}\text{Ra}$ ) has been identified above 2.3 MeV excitation energy and interpreted as two-quasiparticle proton state arising from the  $\pi(h_{9/2}^5 i_{13/2})$  configuration [15,57]. On the other hand, the presence of an odd-spin negative-parity  $E2$  sequence, interleaved with the ground state positive-parity band, in the heavier isotopes (viz.  $^{218}\text{Ra}$ ,  $^{220}\text{Ra}$ ) suggests the onset of octupole collectivity in these nuclei. In  $^{218}\text{Ra}$ , a sharp discontinuity at  $I^\pi = 11^-$  ( $E_x = 2.1$  MeV) is observed in the alignment plot for the negative-parity states [58]. The sudden increase in the alignment above the  $11^-$  state indicates that a band based on the two-quasiparticle proton state ( $11^-$ ), observed in the lighter isotopes, crosses the yrast negative-parity band originating from octupole vibration. Also, the observed decrease in the  $B(E1)/B(E2)$  ratios above this state provides further evidence of noncollective effects in the higher-lying levels [58,59]. It may be noted that no features of band crossing at  $I^\pi = 11^-$  were reported in  $^{220}\text{Ra}$  [58,59]. These observations are consistent with the expected dominance of the collective effects over the single-particle degrees of freedom with the increase in the valence nucleons. Therefore, it may be suggested that the structure above the  $11^-$  and analogous states in the even- and odd- $A$  transitional nuclei, respectively, provide information on the development of octupole collectivity in this region. In  $^{217}\text{Ra}$ , the alternating-parity  $s = -i$  band is observed to terminate at the  $27/2^+$  state and the level structure above this state seems to be dominated by the single-particle excitations. It is interesting to note that a  $29/2^-$  state in  $^{217}\text{Ra}$  is observed at the similar excitation energies as the  $11^-$  states in  $^{216}\text{Ra}$  and  $^{218}\text{Ra}$ . Therefore, the  $29/2^-$  state may be thought of as originating from the coupling of odd particle (hole) in the  $g_{9/2}$  orbital to the  $11^-$  states in  $^{216}\text{Ra}$  ( $^{218}\text{Ra}$ ). Furthermore, the observed structural change in  $^{217}\text{Ra}$  above the  $29/2^-$  level also corroborates the negative parity of the 2301-keV state.

The  $11^-$  state in  $^{216}\text{Ra}$  has the  $\pi(h_{9/2}^5 i_{13/2}) \otimes \nu(g_{9/2}^2)$  configuration [15,39]. The addition of an extra neutron in the  $g_{9/2}$  orbital results in the  $\pi(h_{9/2}^5 i_{13/2}) \otimes \nu(g_{9/2}^3)$  configuration for the  $29/2^-$  state. It may further be noted that the

$13^-$  state in  $^{216}\text{Ra}$  [ $T_{1/2} = 0.96(20)$  ns] decays via an  $E2$  transition of 344 keV to the  $11^-$  level [16,39]. Therefore, the  $33/2^-$  state in  $^{217}\text{Ra}$  at 2394 keV may be realized from the coupling of the odd neutron in the  $g_{9/2}$  orbital to the  $13^-$  state in  $^{216}\text{Ra}$ . The coupling of an extra  $g_{9/2}$  neutron to the dominant configuration of the  $13^-$  level in  $^{216}\text{Ra}$  suggests the  $\pi(h_{9/2}^6) \otimes \nu(g_{9/2} i_{11/2} j_{15/2})$  configuration for the  $33/2^-$  state.

Another possibility is that the  $29/2^-$  and  $33/2^-$  states in  $^{217}\text{Ra}$  originate from the coupling of odd neutron in the  $j_{15/2}$  orbital to the  $8^+$  and  $10^+$  states in  $^{216}\text{Ra}$ , respectively. The  $8^+$  and  $10^+$  states in  $^{216}\text{Ra}$  are associated with the  $\pi(h_{9/2}^6) \otimes \nu(g_{9/2}^2)$  and  $\pi(h_{9/2}^6) \otimes \nu(g_{9/2} i_{11/2})$  configurations, respectively [15,16]. Thus, the addition of the extra neutron in the  $j_{15/2}$  orbital results in the  $\pi(h_{9/2}^6) \otimes \nu(g_{9/2}^2 j_{15/2})$  and  $\pi(h_{9/2}^6) \otimes \nu(g_{9/2} i_{11/2} j_{15/2})$  configurations for the  $29/2^-$  and  $33/2^-$  states in  $^{217}\text{Ra}$ , respectively. Similarly, the coupling of the odd neutron in the  $i_{11/2}$  orbital to the  $11^-$  state in  $^{216}\text{Ra}$  also results in a  $33/2^-$  state in  $^{217}\text{Ra}$  with the configuration  $\pi(h_{9/2}^5 i_{13/2}) \otimes \nu(g_{9/2}^2 i_{11/2})$ . The sequence of the 864-, 371-, and 197 keV transitions above the isomer exhibits the similar trend of decreasing level spacings as observed in the low-lying sequence based on the  $11/2^+$  state. Therefore, the states of this sequence may be understood as originating from the coupling of the  $[\pi(h_{9/2}^5 i_{13/2})_{11^-} \otimes \nu(g_{9/2}^2 i_{11/2})_{11/2^+}]_{33/2^-}$  configuration to the  $\nu(g_{9/2}^2)_{2^+ - 6^+}$  neutron excitations.

## V. SUMMARY

The level structure of the transitional nucleus  $^{217}\text{Ra}$  has been investigated using the  $^{208}\text{Pb}(^{12}\text{C}, 3n)^{217}\text{Ra}$  reaction. The previously reported level scheme is revisited and the placements of several  $\gamma$  rays, which were found to be inconsistent in the earlier studies, have been confirmed in the present work. The addition of a new negative-parity sequence at low excitation energies provides the experimental evidence of parity-doublet structures in  $^{217}\text{Ra}$ , which were earlier reported in all the other  $N = 129$  isotones with  $87 \leq Z \leq 90$ . Although the level spacings in the  $E2$  sequences of the simplex bands do not follow the characteristics of typical rotational bands, the strong  $E1$  connecting transitions and parity doublets suggest the presence of octupole correlations in this nucleus. Therefore, theoretical calculations based on the reflection-asymmetric triaxial particle rotor model have been performed to interpret the observed parity-doublet structures. The calculated energies were found to be in reasonable agreement with the experimental results in the spin range  $9/2 \hbar \leq I \leq 21/2 \hbar$  for the positive-parity states and  $13/2 \hbar \leq I \leq 27/2 \hbar$  for the negative-parity states. The properties [energy splitting,  $I(\omega)$  and  $B(E1)/B(E2)$  ratios] of the simplex bands in  $^{217}\text{Ra}$  are also compared with that of the similar bands in neighboring nuclei and the results of the RAT-PRM calculations. The observed structures at low excitation energies reflect an intermediate behavior between the extremes of single-particle excitations and stable octupole deformation. Furthermore, it is observed that the simplex bands in  $^{217}\text{Ra}$  terminate at the intermediate excitation energies, unlike  $^{218}\text{Ra}$  where the alternating-parity sequence persist up to the

maximum observed spin. Also, the level structures above the  $29/2^-$  state in  $^{217}\text{Ra}$  appear to be mainly governed by single-particle excitations. Finally, it may be noted that the competing single-particle and collective degrees of freedom govern the structure in different energy regimes of this nucleus.

### ACKNOWLEDGMENTS

The authors thank the staff of IUAC target laboratory for facilitating the preparation of the target. The authors gratefully acknowledge the IUAC support staff for their assistance during the experiment. The financial support by

DST, India (Grant No. IR/S2/PF-03/2003-III) for the INGA project is acknowledged. The authors also thank INGA collaboration for their help and support. Madhu acknowledges the financial support from DST, India under the INSPIRE fellowship scheme (IF 180082). A.Y.D. and D.S. acknowledge the financial support by SERB (DST) vide Grant No. CRG/2020/002169. K.Y. acknowledges the support from the Ministry of Human Resource Development, India. Y.Y.W., Y.K.W., and J.M. acknowledge the support from the National Natural Science Foundation of China (Grants No. 12141501, No. 12205097, and No. 11935003), and the High-performance Computing Platform of Peking University.

- 
- [1] I. Ahmad and P. A. Butler, *Annu. Rev. Nucl. Part. Sci.* **43**, 71 (1993), and references therein.
- [2] P. A. Butler and W. Nazarewicz, *Rev. Mod. Phys.* **68**, 349 (1996).
- [3] S. C. Pancholi, *Pear-Shaped Nuclei* (World Scientific, Singapore, 2020).
- [4] H. J. Wollersheim, H. Emling, H. Grein, R. Kulesa, R. S. Simon, C. Fleischmeann, J. de Boer, E. Hauber, C. Lauterbach, C. Schandera, P. A. Butler, and T. Czosnyka, *Nucl. Phys. A* **556**, 261 (1993).
- [5] L. P. Gaffney *et al.*, *Nature (London)* **497**, 199 (2013).
- [6] P. A. Butler, L. P. Gaffney, P. Spagnoletti, K. Abrahams, M. Bowry, J. Cederkäll *et al.*, *Phys. Rev. Lett.* **124**, 042503 (2020).
- [7] B. Bucher, S. Zhu, C. Y. Wu, R. V. F. Janssens, D. Cline, A. B. Hayes *et al.*, *Phys. Rev. Lett.* **116**, 112503 (2016).
- [8] B. Bucher, S. Zhu, C. Y. Wu, R. V. F. Janssens, R. N. Bernard, L. M. Robledo *et al.*, *Phys. Rev. Lett.* **118**, 152504 (2017).
- [9] P. A. Butler, *Proc. R. Soc. A* **476**, 20200202 (2020).
- [10] S. Frauendorf, *Rev. Mod. Phys.* **73**, 463 (2001).
- [11] W. Reviol, C. J. Chiara, M. Montero, D. G. Sarantites, O. L. Pechenaya, M. P. Carpenter, R. V. F. Janssens, T. L. Khoo, T. Lauritsen, C. J. Lister, D. Seweryniak, S. Zhu, and S. G. Frauendorf, *Phys. Rev. C* **74**, 044305 (2006).
- [12] W. Reviol *et al.*, *Acta Phys. Pol. B* **42**, 671 (2011).
- [13] W. Reviol, D. G. Sarantites, C. J. Chiara, M. Montero, R. V. F. Janssens, M. P. Carpenter, T. L. Khoo, T. Lauritsen, C. J. Lister, D. Seweryniak, S. Zhu, O. L. Pechenaya, and S. G. Frauendorf, *Phys. Rev. C* **80**, 011304(R) (2009).
- [14] S. Frauendorf, *Phys. Rev. C* **77**, 021304(R) (2008).
- [15] T. Lönnroth, D. Horn, C. Baktash, and C. J. Lister, and G. R. Young, *Phys. Rev. C* **27**, 180 (1983).
- [16] S. Muralithar, G. Rodrigues, R. P. Singh, R. K. Bhowmik, P. Mukherjee, B. Sethi, and I. Mukherjee, *Pramana-J. Phys.* **79**, 403 (2012).
- [17] N. Schulz, V. Vanin, M. Aïche, A. Chevallier, J. Chevallier, J. C. Sens, Ch. Briangon, S. Cwiok, E. Ruchowska, J. Fernandez-Niello, Ch. Mittag, and J. Dudek, *Phys. Rev. Lett.* **63**, 2645 (1989).
- [18] N. Roy, D. J. Decman, H. Kluge, K. H. Maier, A. Maj, C. Mittag, J. Fernandez-Niello, H. Puchta, and F. Riess, *Nucl. Phys. A* **426**, 379 (1984).
- [19] M. Sugawara, Y. Gono, and Y. Itoh, *J. Phys. Soc. Jpn.* **53**, 2956 (1984).
- [20] M. Sugawara, Y. Gono, T. Kohno, and M. Fukuda, *RIKEN Accel. Prog. Rep.* **20**, 12 (1986).
- [21] S. Muralithar, Ph.D. thesis, Jawaharlal Nehru University, 2011.
- [22] E. Parr, J. F. Smith, P. T. Greenlees, K. Auranen, R. Chapman, D. M. Cullen *et al.*, *Phys. Rev. C* **102**, 054335 (2020), and references therein.
- [23] A. Lopez-Martens, K. Hauschild, K. Rezykina, O. Dorvaux, B. Gall, F. Dechery, H. Faure, A. V. Yeremin, M. L. Chelnokov, V. I. Chepigin, A. V. Isaev, I. N. Izosimov, D. E. Katrasev, A. N. Kuznetsov, A. A. Kuznetsova, O. N. Malyshev, A. G. Popeko, E. A. Sokol, A. I. Svirikhin, J. Piot *et al.*, *Eur. Phys. J. A* **50**, 132 (2014).
- [24] W. Hua, Z. Zhang, L. Ma, Z. Gan, H. Yang, M. Huang, C. Yang, M. Zhang, Y. Tian, X. Zhou, C. Yuan, C. Shen, and L. Zhu, *Chin. Phys. C* **45**, 044003 (2021).
- [25] Pragati, A. Y. Deo, S. K. Tandel, S. S. Bhattacharjee, S. Chakraborty, S. Rai, S. G. Wahid, S. Kumar, S. Muralithar, R. P. Singh, I. Bala, R. Garg, and A. K. Jain, *Phys. Rev. C* **97**, 044309 (2018).
- [26] M. E. Debray, A. J. Kreiner, M. Davidson, J. Davidson, D. Hojman, D. Santos, V. R. Vanin, N. Schulz, M. Aiche, A. Chevallier, J. Chevallier, and J. C. Sens, *Nucl. Phys. A* **568**, 141 (1994).
- [27] S. Muralithar *et al.*, *J. Phys.: Conf. Ser.* **312**, 052015 (2011).
- [28] M. Jain, E. T. Subramaniam, and S. Chatterjee, *Rev. Sci. Instrum.* **94**, 013304 (2023).
- [29] R. Brun and F. Rademakers, *Nucl. Instrum. Methods Phys. Res., Sec. A* **389**, 81 (1997).
- [30] A. Z. Schwarzschild and E. K. Warburton, *Annu. Rev. Nucl. Sci.* **18**, 265 (1968).
- [31] A. Krämer-Flecken, T. Morek, R. M. Lieder, W. Gast, G. Hebbinghaus, H. M. Jäger, and W. Urban, *Nucl. Instrum. Methods Phys. Res., Sec. A* **275**, 333 (1989).
- [32] G. Duchêne, F. A. Beck, P. J. Twin, G. de France, D. Kurien, L. Han, C. W. Beausang, M. A. Bentley, P. J. Nolan, and J. Simpson, *Nucl. Instrum. Methods Phys. Res., Sec. A* **432**, 90 (1999).
- [33] K. Starosta, T. Morek, Ch. Droste, S. G. Rohoziński, J. Srebrny, A. Wierzchucka, M. Bergström, B. Herskind, E. Melby, T. Czosnyka, and P. J. Napiorkowski, *Nucl. Instrum. Methods Phys. Res., Sec. A* **423**, 16 (1999).
- [34] T. Yamazaki, *Nucl. Data, Sec. A* **3**, 1 (1967).
- [35] E. der Mateosian and A. W. Sunyar, *At. Data Nucl. Data Tables* **13**, 391 (1974).
- [36] R. Palit, H. C. Jain, P. K. Joshi, S. Nagaraj, B. V. T. Rao, S. N. Chintalapudi, and S. S. Ghugre, *Pramana* **54**, 347 (2000).

- [37] K. Yadav, A. Y. Deo, Madhu, Pragati, P. C. Srivastava, S. K. Tandel, S. G. Wahid, S. Kumar, S. Muralithar, R. P. Singh, I. Bala, S. S. Bhattacharjee, R. Garg, S. Chakraborty, S. Rai, and A. K. Jain, *Phys. Rev. C* **105**, 034307 (2022).
- [38] F. G. Kondev, E. A. McCutchan, B. Singh, K. Banerjee, S. Bhattacharya, A. Chakraborty, S. Garg, N. Jovancevic, S. Kumar, S. K. Rathi, T. Roy, J. Lee, and R. Shearman, *Nucl. Data Sheets* **147**, 382 (2018).
- [39] G. D. Dracoulis, F. Riess, A. M. Baxter, and A. E. Stuchbery, *J. Phys. G: Nucl. Part. Phys.* **17**, 1795 (1991).
- [40] R. K. Sheline, C. F. Liang, P. Paris, A. Gizon, and V. Barci, *Phys. Rev. C* **49**, 725 (1994).
- [41] W. Nazarewicz, P. Olanders, I. Ragnarsson, J. Dudek, and G. A. Leander, *Phys. Rev. Lett.* **52**, 1272 (1984).
- [42] G. Maquart, L. Augey, L. Chaix, I. Companis, C. Ducoin, J. Dudouet *et al.*, *Phys. Rev. C* **95**, 034304 (2017).
- [43] M. E. Debray, M. A. Cardona, D. Hojman, A. J. Kreiner, M. Davidson, J. Davidson, H. Somacal, G. Levinton, D. R. Napoli, S. Lenzi, G. de Angelis, M. De Poli, A. Gadea, D. Bazzacco, C. Rossi-Alvarez, and N. Medina, *Phys. Rev. C* **62**, 024304 (2000).
- [44] T. C. Hensley, P. D. Cottle, V. Tripathi, B. Abromeit, M. Anastasiou, L. T. Baby, J. S. Baron, D. Caussyn, R. Dungan, K. W. Kemper, R. S. Lubna, S. L. Miller, N. Rijal, M. A. Riley, S. L. Tabor, P.-L. Tai, and K. Villafana, *Phys. Rev. C* **96**, 034325 (2017).
- [45] N. Schulz, V. R. Vanin, A. J. Kreiner, E. Ruchowska, M. Aiche, Ch. Briangon, A. Chevallier, J. Chevallier, M. E. Debray, and J. C. Sens, *Z. Phys. A* **339**, 325 (1991).
- [46] W. Reviol, R. V. F. Janssens, S. Frauendorf, D. G. Sarantites, M. P. Carpenter, X. Chen, C. J. Chiara, D. J. Hartley, K. Hauschild, T. Lauritsen, A. Lopez-Martens, M. Montero, O. L. Pechenaya, D. Seweryniak, J. B. Snyder, and S. Zhu, *Phys. Rev. C* **90**, 044318 (2014).
- [47] Y. Y. Wang, S. Q. Zhang, P. W. Zhao, and J. Meng, *Phys. Lett. B* **792**, 454 (2019).
- [48] Y. P. Wang, Y. Y. Wang, and J. Meng, *Phys. Rev. C* **102**, 024313 (2020).
- [49] Y. Y. Wang and S. Q. Zhang, *Phys. Rev. C* **102**, 034303 (2020).
- [50] Y. Y. Wang, X. H. Wu, S. Q. Zhang, P. W. Zhao, and J. Meng, *Sci. Bull.* **65**, 2001 (2020).
- [51] Y. Y. Wang, Q. B. Chen, and S. Q. Zhang, *Phys. Rev. C* **105**, 044316 (2022).
- [52] P. Möller, R. Bengtsson, B. G. Carlsson, P. Olivius, T. Ichikawa, H. Sagawa, and A. Iwamoto, *At. Data Nucl. Data Tables* **94**, 758 (2008).
- [53] Y. Y. Wang and Z. X. Ren, *Sci. China Phys. Mech. Astron.* **61**, 082012 (2018).
- [54] G. A. Leander, W. Nazarewicz, G. F. Bertsch, and J. Dudek, *Nucl. Phys. A* **453**, 58 (1986).
- [55] P. Ring and P. Schuck, *The Nuclear Many-Body Problem* (Springer-Verlag, Berlin, 1980).
- [56] Y. Y. Wang, *Phys. Rev. C* **104**, 014318 (2021).
- [57] A. E. Stuchbery, G. D. Dracoulis, T. Kibédi, A. P. Byrne, B. Fabricius, A. R. Poletti, G. J. Lane, and A. M. Baxter, *Nucl. Phys. A* **548**, 159 (1992).
- [58] J. F. Shriner, Jr., P. D. Cottle, J. F. Ennis, M. Gai, D. A. Bromley, J. W. Olness, E. K. Warburton, L. Hildingsson, M. A. Quader, and D. B. Fossan, *Phys. Rev. C* **32**, 1888 (1985).
- [59] P. D. Cottle, J. F. Shriner, Jr., F. Dellagiacoma, J. F. Ennis, M. Gai, D. A. Bromley, J. W. Olness, E. K. Warburton, L. Hildingsson, M. A. Quader, and D. B. Fossan, *Phys. Rev. C* **30**, 1768(R) (1984).